

## Evidence for Extended Hydrogen-Poor CSM in the Three-Peaked Light Curve of Stripped Envelope Ib Supernova

YOSSEF ZENATI,<sup>1,\*</sup> QINAN WANG,<sup>1</sup> ALEXEY BOBRICK,<sup>2</sup> LINDSAY DEMARCHI,<sup>3</sup> HILA GLANZ,<sup>2</sup> MOR ROZNER,<sup>2</sup> ARMIN REST,<sup>4,1</sup>  
BRIAN D. METZGER,<sup>5,6</sup> RAFFAELLA MARGUTTI,<sup>7</sup> SEBASTIAN GOMEZ,<sup>4</sup> NATHAN SMITH,<sup>8</sup> SILVIA TOONEN,<sup>9</sup> JOE S. BRIGHT,<sup>10,11</sup>  
COLIN NORMAN,<sup>1,4</sup> RYAN J. FOLEY,<sup>12</sup> ALEXANDER GAGLIANO,<sup>13,14,15,†</sup> JULIAN H. KROLIK,<sup>1</sup> STEPHEN J. SMARTT,<sup>16</sup>  
ASHLEY V. VILLAR,<sup>17,18,19</sup> GAUTHAM NARAYAN,<sup>13,14,15</sup> ORI FOX,<sup>4</sup> KATIE AUCHETTL,<sup>12,20,21</sup> DANIEL BRETHAUER,<sup>7</sup>  
ALEJANDRO CLOCCHIATTI,<sup>22,23</sup> SOPHIE V. COELLN,<sup>1</sup> DEANNE L. COPPEJANS,<sup>24</sup> GEORGIOS DIMITRIADIS,<sup>25</sup> ANDRIS DOROSZMAI,<sup>9</sup>  
MARIA DROUT,<sup>26,27</sup> WYNN JACOBSON-GALAN,<sup>7</sup> BORE GAO,<sup>1</sup> RYAN RIDDEN-HARPER,<sup>28</sup> CHARLES DONALD KILPATRICK,<sup>3</sup> TANMOY LASKAR,<sup>29</sup>  
DAVID MATTHEWS,<sup>7</sup> SOFIA REST,<sup>1</sup> KEN W. SMITH,<sup>30</sup> CANDICE MCKENZIE STAUFFER,<sup>3</sup> MICHAEL C. STROH,<sup>3</sup> LOUIS-GREGORY STROLGER,<sup>4</sup>  
GIACOMO TERRERAN,<sup>3</sup> JUSTIN D. R. PIEREL,<sup>4</sup> AND ANTHONY L. PIRO<sup>31</sup>

<sup>1</sup>*Physics and Astronomy Department, Johns Hopkins University, Baltimore, MD 21218, USA*

<sup>2</sup>*Technion - Israel Institute of Technology, Physics department, Haifa Israel 3200002*

<sup>3</sup>*Center for Interdisciplinary Exploration and Research in Astrophysics (CIERA) and Department of Physics and Astronomy, Northwestern University, Evanston, IL 60208*

<sup>4</sup>*Space Telescope Science Institute, 3700 San Martin Dr., Baltimore, MD 21218, USA*

<sup>5</sup>*Department of Physics and Columbia Astrophysics Laboratory, Columbia University, Pupin Hall, New York, NY 10027, USA*

<sup>6</sup>*Center for Computational Astrophysics, Flatiron Institute, 162 5th Ave, New York, NY 10010, USA*

<sup>7</sup>*Department of Astronomy and Astrophysics, University of California, Berkeley, CA 94720, USA*

<sup>8</sup>*Steward Observatory, University of Arizona, 933 N. Cherry Avenue, Tucson, AZ 85721, USA*

<sup>9</sup>*Anton Pannekoek Institute for Astronomy, University of Amsterdam, 1090 GE Amsterdam, The Netherlands*

<sup>10</sup>*Department of Astronomy, University of California, Berkeley, CA 94720-3411, USA*

<sup>11</sup>*Astrophysics, Department of Physics, University of Oxford, Keble Road, Oxford OX1 3RH, UK*

<sup>12</sup>*Department of Astronomy and Astrophysics, University of California, Santa Cruz, CA 95064, USA*

<sup>13</sup>*Department of Astronomy, University of Illinois at Urbana-Champaign, 1002 W. Green St, IL 61801, USA*

<sup>14</sup>*Center for Astrophysical Surveys, National Center for Supercomputing Applications, Urbana, IL 61801, USA*

<sup>15</sup>*Center for Astrophysical Surveys, Urbana, IL 61801, USA*

<sup>16</sup>*Astrophysics Research Centre, School of Mathematics and Physics, Queens University Belfast, Belfast BT7 1NN, UK*

<sup>17</sup>*Department of Astronomy and Astrophysics, Pennsylvania State University, 525 Davey Laboratory, University Park, PA 16802, USA*

<sup>18</sup>*Institute for Computational & Data Sciences, The Pennsylvania State University, University Park, PA, USA*

<sup>19</sup>*Institute for Gravitation and the Cosmos, The Pennsylvania State University, University Park, PA 16802, USA*

<sup>20</sup>*School of Physics, The University of Melbourne, VIC 3010, Australia*

<sup>21</sup>*ARC Centre of Excellence for All Sky Astrophysics in 3 Dimensions (ASTRO 3D), Australia*

<sup>22</sup>*Instituto de Astrofísica, Pontificia Universidad Católica, Vicuña Mackenna 4860, 7820436 Santiago, Chile*

<sup>23</sup>*Millennium Institute of Astrophysics, Nuncio Monseñor ~ Sótero Sanz 100, Of. 104, Providencia, 7500000 Santiago, Chile*

<sup>24</sup>*Department of Physics, University of Warwick, Coventry CV4 7AL, UK*

<sup>25</sup>*School of Physics, Trinity College Dublin, The University of Dublin, Dublin 2, Ireland*

<sup>26</sup>*David A. Dunlap Department of Astronomy and Astrophysics, University of Toronto, 50 St. George Street, Toronto, Ontario, M5S 3H4, Canada*

<sup>27</sup>*Observatories of the Carnegie Institution for Science, 813 Santa Barbara Street, Pasadena, CA 91101, USA*

<sup>28</sup>*School of Physical and Chemical Sciences | Te Kura Matū, University of Canterbury, Private Bag 4800, Christchurch 8140, New Zealand*

<sup>29</sup>*Department of Astrophysics/IMAPP, Radboud University, PO Box 9010, 6500 GL, The Netherlands*

<sup>30</sup>*Astrophysics Research Centre, School of Mathematics and Physics, Queen's University Belfast, Belfast, BT7 1NN, UK*

<sup>31</sup>*The Observatories of the Carnegie Institution for Science, 813 Santa Barbara St., Pasadena, CA 91101, USA*

### ABSTRACT

1 We present multi-band ATLAS photometry for SN 2019tsf, a stripped-envelope Type Ib supernova (SESN).  
2 The SN shows a triple-peaked light curve and a late (re-)brightening, making it unique among stripped-envelope  
3 systems. The re-brightening observations represent the latest photometric measurements of a multi-peaked  
4 Type Ib SN to date. As late-time photometry and spectroscopy suggest no hydrogen, the potential circumstellar  
5 material (CSM) must be H-poor. Moreover, late (>150 days) spectra show no signs of narrow emission lines,

further disfavoring CSM interaction. On the contrary, an extended CSM structure is seen through a follow-up radio campaign with Karl G. Jansky Very Large Array (VLA), indicating a source of bright optically thick radio emission at late times, which is highly unusual among H-poor SESNe. We attribute this phenomenology to an interaction of the supernova ejecta with spherically-asymmetric CSM, potentially disk-like, and we present several models that can potentially explain the origin of this rare Type Ib supernova. The warped disc model paints a novel picture, where the tertiary companion perturbs the progenitors CSM, that can explain the multi-peaked light curves of SNe, and here we apply it to SN 2019tsf. This SN 2019tsf is likely a member of a new sub-class of Type Ib SNe and among the recently discovered class of SNe that undergo mass transfer at the moment of explosion.

*Keywords:* supernovae:general — supernovae: individual (SN 2019tsf)— common envelope — nuclear reactions — nucleosynthesis

## 1. INTRODUCTION

There is significant observational diversity among stripped-envelope supernovae (SESNe), systems defined by the absence of H and He as inferred from spectroscopy. Following the SN classification scheme (Ia, Ib/c, II, etc) developed during the last three decades, these events can be H-poor and He-rich (SN Ib); H-poor and He-poor (SN Ic); or somewhere in between, with early H- $\alpha$  lines that fade with time (I Ib SNe, (Dessart et al. 2012; Yoon 2015; Prentice & Mazzali 2017; Prentice et al. 2019)). Based on the light curve, the typical time scale for the first peak of SNe Ib, thought to be powered by the radioactive decay of  $^{56}\text{Ni}$ , is  $\sim 20 - 25$  days (Dessart et al. 2011; Taddia et al. 2015). The light curves of SNe Ic, whose progenitors lack both their hydrogen and their helium envelopes, evolve in a manner similar to traditional SNe Ia but are  $\sim 1$  mag fainter at peak. These events are more common than SNe IIb; SNe Ib/c comprise  $\sim 19\%$  of all SNe and  $\sim 26\%$  of all core collapse SNe (CCSNe) (Smith et al. 2011b), relative to  $\sim 5\text{-}10\%$  of SNe II for SNe IIb (e.g. (Arcavi et al. 2011; Smith et al. 2011a; Claeys et al. 2011; Sana et al. 2012a; Gal-Yam 2017; Fang et al. 2022)). SNe IIb light curves may exhibit early bumps from the interaction of the SN shock or more slower-moving ejecta with surrounding CSM. If the interaction of the shock wave with the CSM is particularly strong, the SN may be also be classified as a SN Ibn (e.g., SN2006jc, SN2014av); these may be analogous to SNe IIn with H-poor interacting CSM, exhibiting narrow Balmer series emission lines. The light curves of these events are distinct among SNe, with peaks near  $\sim -19$  mag and a rapid decline  $\sim 0.1\text{mag/day}$  (Foley et al. 2007; Pastorello et al. 2016; Smith 2017; Hosseinzadeh et al. 2019). More recently, Gal-Yam et al. (2022) introduced the SN Icn class to refer to objects that are lacking in hydrogen and helium, but show strong narrow emission lines of carbon or oxygen (e.g., Pellegrino et al. 2022; Perley et al. 2022). Finally, Type I superluminous supernovae (SLSN-I) are a class of stripped envelope core-collapse SNe characterized by their blue spectra and high luminosity, peaking at magnitudes brighter than

$\sim -19.8$  mag (Chomiuk et al. 2011; Quimby et al. 2011; Villar et al. 2018; Gomez et al. 2021).

Because the photometric and spectroscopic signatures of these systems are directly linked to the behavior of their progenitors in the pre-explosion phase, a thorough understanding of the diversity of SESN observations is paramount to uncovering the dynamic ecosystem of pathways that lead to stellar death. This diversity cannot be fully understood by the underlying  $^{56}\text{Ni}$  mass synthesized in the explosion; SNe Ib/c and SNe II both produce  $\lesssim 0.03 - 0.1M_{\odot}$  of  $^{56}\text{Ni}$  (Anderson 2019), yet exhibit dramatically different photometric and spectroscopic evolution. Radioactive  $^{56}\text{Ni}$  may not be the sole heating source for these enigmatic events: (Ertl et al. 2019) find that the  $^{56}\text{Ni}$  amount of SESN progenitor models are inadequate to give rise for the peak luminosities of  $\sim$  half of ordinary Type Ib/c.

Despite the numerous questions that remain in the effort to link SESN to their pre-explosion counterparts, growing samples have constrained the parameter space of viable explosion mechanisms for specific classes. Generally, there are two main channels thought to give rise to SNe Ib/c. One channel is the mass loss from single massive stars via strong stellar winds or an unstable envelope. In this case, the progenitor is a Wolf-Rayet star (WR) (Woosley et al. 1993; Georgy et al. 2009; Tramper et al. 2015; Dessart et al. 2020) (further details about the connection between SN Ib, Ic and the WR in its different stages as, WNL, WNE, WC, and WO stars can be found in Georgy et al. (2009)). Another channel is binary interaction, which would require a close binary that ends its stellar evolution as a pair of young, massive stars (Yoon et al. 2010; Smith et al. 2011a; Sana et al. 2012a; Ben-Ami et al. 2014; Dessart et al. 2015; Rimoldi et al. 2016; Janssens et al. 2021). Most recently, Fox et al. (2022) discovered the first surviving companion to a Type Ib/c in the case of SN 2013ge could be explained by binary models which tend to predict OB-type stars. Other more exotic scenarios have also been proposed for SLSNe-I; one theory consists of the collapsar model of a rapidly-rotating star whose hydrogen envelope has been stripped during the pre-explosion time, which minimizes the chances that could explain the majority of SN Ib/c. (MacFadyen & Woosley 1999; Woosley & Bloom 2006; Nicholl et al. 2017; Nagataki 2018; Zenati et al. 2020; Lee et al. 2022).

\* CHE Israel Excellence Fellowship

† National Science Foundation Graduate Research Fellow

Multi-wavelength follow-up is uniquely valuable for understanding the explosion mechanisms of SESNe. Broad-lined SNe Ic (SNe Ic-BL), a subclass of SNe Ic with high expansion velocities and low host galaxy metallicities, remain the only supernova class to be unambiguously associated with long-duration gamma-ray bursts (LGRBs), whose gamma-ray emission lasts longer than  $\sim 2$  seconds (Modjaz et al. 2019). As LGRBs accompany an explosion in the collapsar model for progenitor stripping, the absence of these signals or the associated afterglows in traditional SN Ib/c disfavors this theory for explaining the majority of SNe Ib/c. Iwamoto et al. (1999) showed that the spectra of extremely energetic events ( $E_k \sim 10^{52} \text{ erg}$ ) are also accompanied by X-ray flashes (XRF) could be the progenitor of those association SNe with the LGRBs.

When obtaining multi-wavelength follow-up, full-phase coverage of the event is the key to providing a comprehensive picture of an explosion. Moderate cadence data can reveal distinct stages of an explosion, including its first emission in SNe Ia (e.g., Wang et al. 2021), and shock-breakout in type-II SNe (Bersten et al. 2018). SESNe can show two prominent peaks in their optical light curves (Roy et al. 2016; Gomez et al. 2019): a burst of emission after the initial explosion, known as the shock cooling light curve (Arcavi et al. 2017; Gal-Yam 2017), and the radioactive decay of  $^{56}\text{Ni}$  to  $^{56}\text{Co}$  and then  $^{56}\text{Co}$  to  $^{54}\text{Fe}$  that powers the emission over the bulk of its lifetime and in late-time the rebrightening occurs due to CSM interaction.

In the last decade, transient surveys of increased sensitivity and depth have discovered SESNe with unprecedented photometric behavior. This has included the ultra-bright SLSNe-I and the ultra-rapid Fast Blue Optical Transients (FBOTs), the latter having a rise time to peak of less than 10 days and a rapid fast decreasing exponential decline lasting  $\sim 30$  days. Recently, (Metzger 2022) discussed a peculiar and extremely rare luminous FBOT subclass (LFBOTs). There are indications that these unique phenomena are realizations along a spectrum of non-standard interactions between SN ejecta and the surrounding CSM (Kasen 2017; Leung et al. 2021). Because CSM is swept up as the SN shock and subsequent ejecta expand, these unusual light curve signatures offer an insightful window into the environments of SN progenitors at the moment of stellar death.

Here, we present optical and radio observations of SN 2019tsf, a SESN event with a remarkably unique light curve evolution. SN 2019tsf was originally classified as an SN Ib by (Sollerman et al. 2020), and two distinct peaks were clearly observed in the ZTF light curve: an initial peak (unfortunately at the beginning of observations) and a late-phase peak observed 90 days later. However, a third peak was uniquely observed by ATLAS due to extended coverage of the object, as shown later in this paper.

This evolution is distinct from any previously-observed SNe Ib/c. Moreover, the spectra of SN 2019tsf has no discernible narrow-line hydrogen signatures that are typically the hallmark of CSM interactions. Optical observations of SN 2019tsf extend over 430 days and reveal at least three well-

resolved peaks until 180 days, during which the luminosity varies by as much as 50%. Instead of lines of hydrogen formed by the explosion or the CSM interaction, spectroscopic follow-up of SN 2019tsf showed only weak hydrogen lines and a small fraction of helium.

In this paper, we first present ATLAS and late-phase DECam observations of SN 2019tsf and suggest theoretical scenarios to explain these light curves and spectra out to  $\sim 400$  days after the first detection. Moreover, we present the first epoch of radio observation of the SE SN 2019tsf. This epoch of radio observations allows us to build up a picture of the underlying physics of this phenomenon.

In §2, we present the optical observations and the data reduction of SN 2019tsf. In §3, we present the Karl G. Jansky Very Large Array (VLA) observations and constrain the physical properties of the radio emitting region with synchrotron modeling of the emission.

In §5, we present modeling of stellar evolution of SN 2019tsf and the bands light curve evolution and derive physical properties of the radioactive decay-powered explosion, magnetar, warped disc scenario, and the ejecta running in disc and the interaction between SN ejecta and the CSM. In §6, we discuss how SN 2019tsf compares to other late-time SN light curves and how these new observations constrain the SN progenitor system. In §7, we summarize our study with recommendation for future follow up of the SESN like SN 2019tsf.

In this paper, observed times are reported in Modified Julian Days (MJDs). We adopt the AB magnitude system, unless where noted, and a flat  $\Lambda$ CDM cosmological model with  $H_0 = 73 \text{ km s}^{-1} \text{ Mpc}^{-1}$  (Riess et al. 2016, 2018).

## 2. OPTICAL OBSERVATIONS

Photometric observations of SN 2019tsf were conducted with a variety of ground-based telescopes from MJD 58788.64 to MJD 59265.25 (within  $\sim 470$  days after the first detection in ZTF). As discussed in Sollerman et al. (2020), the host galaxy of SN 2019tsf, NGC 3541, has a well established redshift of  $z = 0.021$ , and we adopt this value throughout this paper. The first detection and also the first peak in ATLAS-*o* band was taken on  $t_{peak_o} = 58788.64$  days (MJD) with a magnitude of  $17.34 \pm 0.04 \text{ mag}$ ,  $\sim 3$  days after first detection in ZTF-*r* band (MJD 58785.53). The last non-detection of ATLAS-*o* appeared on MJD 58642.27 below  $20.43 \text{ mag}$ .

We obtained archival photometric measurements from ZTF in *g* and *r* filters from Sollerman et al. (2020). SN 2019tsf was also observed by ATLAS, a twin 0.5m telescope system installed on Haleakala and Mauna Loa in the Hawaiian islands, in cyan (*c*) and orange (*o*) filters (Tonry et al. 2018a). The ATLAS images are processed as described in Tonry et al. (2018a), and then photometrically and astrometrically calibrated using the RefCat2 catalogue (Tonry et al. 2018b). Template generation, image subtraction procedures and photometric measurements are carried out following (Smith et al. 2020).

The photometry presented here are weighted averages of the nightly individual 30 sec exposures, carried out with forced

**Table 1.** Main parameters of SN 2019tsf and its host galaxy

Host Galaxy	NGC 3541
Redshift	$0.02093 \pm 0.00003^a$
Distance	83.90 Mpc
Distance Modulus, $\mu$	$34.62 \pm 0.54$ mag
RA <sub>SN</sub>	$11^{\text{h}}08^{\text{m}}32.80^{\text{s}}$
Dec <sub>SN</sub>	$-10^{\circ}28'54.4''$
$E(B - V)_{\text{MW}}$	$0.024 \pm 0.001$ mag <sup>b</sup>
Time of First $o$ -band Peak (MJD)	$58788.65 \pm 0.01$
$m_o^{\text{peak}}$	$17.34 \pm 0.04$ mag
$M_o^{\text{peak}}$	$-17.28 \pm 0.54$ mag

<sup>a</sup> Springob et al. (2014)

<sup>b</sup> Schlegel et al. (1998); Schlafly & Finkbeiner (2011)

photometry at the position of the SNe, as shown in Figure 2(a). We obtained additional late-time, ground-based imaging of SN 2019tsf  $\sim 300$  days after explosion in  $r$ - and  $i$ -band with DECam through the DECam Extension of the Young Supernova Experiment (Rest et al. 2022). We obtained two spectra with the ESO Faint Object Spectrograph and Camera (EFOSC2; Buzzoni et al. 1984) on the ESO New Technology Telescope (as part of the ePESSTO survey, (Smartt et al. 2015)) around MJD 58792.35 and 58892.25, roughly  $\sim 4$  and 100 days after the first peak in rest frame, as shown in Figure. 3.

We also present new late time spectra of SN 2020oi and SN 2019yvr from Shane telescope. The spectra were reduced using standard IRAF/PYRAF<sup>1</sup> and python routines for bias/overscan subtractions and flat fielding. The wavelength solution was derived using arc lamps while the final flux calibration and telluric lines removal were performed using spectro-photometric standard star spectra.

### 3. RADIO OBSERVATIONS AND MODELING

#### 3.1. Karl G. Jansky Very Large Array Observations

We observed the field of SN 2019tsf with the Karl G. Jansky Very Large Array (VLA) beginning on 2022 January 21 (MJD 59612.29) or  $\delta t = 811.68$  days after the ATLAS-o detection (MJD 58788.64) as part of program VLA/21A-239 (PI DeMarchi). Observations were taken at S-, C-, X-, Ku- and K-band, utilizing the WIDAR correlator for maximum sensitivity. The data were reduced using the VLA pipeline in the Common Astronomy Software Applications package (CASA, McMullin et al. 2007) pipeline version 2020.1.0.36 (CASA version 6.1.2.7) followed by manual inspection, flag-

ging and reprocessing through the imaging pipeline. For the data taken at C, X and Ku band we used the image product produced by the pipeline and fit the source using the CASA task `IMFIT`. At S-band, where the source was faintest and corrupting field sources were more prevalent, we applied phase and amplitude self-calibration with a scan based solution interval to improve the image noise at the target location, which revealed a marginal detection of the target. Our observations are detailed in Table 2, and plotted in Figure 5.

#### 3.2. Radio Modelling

In a SN explosion, optical observations sample the slowly expanding ejecta ( $v \leq 10^4$  km s<sup>-1</sup>) emitting thermal radiation, while radio observations measure radio synchrotron emission from the fastest ejecta ( $v \geq 0.1c$ ). Radio synchrotron emission originates from the interaction of the fastest SN ejecta with the local CSM, itself shaped by the mass loss of the progenitor star prior to explosion. For the typical radio SN, the result is a bell-shaped spectral energy distribution (SED), with the spectral peak  $\nu_{\text{pk}}$  cascading to lower radio frequencies with time as the blastwave expands and the ejecta become optically thin to synchrotron self-absorption (SSA) and free-free absorption (FFA). For the typical radio SN,  $\nu_{\text{pk}}$  corresponds to the SSA frequency  $\nu_{\text{sa}}$ . Under these assumptions, by monitoring  $\nu_{\text{sa}}(t)$  and the peak flux density  $F_{\text{pk}}(t)$ , we can directly constrain the forward-shock radius  $R(t)$  and the post-shock magnetic field  $B(t)$ , from which the pre-shock CSM density  $\rho_{\text{CSM}}$  and mass-loss rate  $\dot{M}$  can be derived (e.g., Chevalier 1998; Chevalier & Fransson 2017).

Here we use the equations presented in DeMarchi et al. (2022), which were derived from Chevalier (1998). In our calculations, we assume that the fraction of total blastwave internal energy  $\rho_{\text{CSM}}v_{\text{sh}}^2$  (where  $v_{\text{sh}} \equiv dR/dt$ , the forward shock velocity) imparted to relativistic electrons is  $\epsilon_e = 0.1$  and that the post-shock magnetic energy fraction is  $\epsilon_B = 0.01$ . We assume a power-law evolution of the forward-shock radius  $R$  as a function of time  $t$ , such that  $R \propto t^q$ . However, because the optically thin portion of the spectrum is not observed, we cannot measure  $R(t)$  directly. Instead, we adopt  $q = 0.88$  as in Chevalier (1982) for the case of a stripped-envelope SN shock launched by a compact massive star interacting with a CSM wind-density profile. We are thus able to obtain constraints on the CSM density around the explosion, littered by the mass-loss history of the progenitor star in the centuries before core collapse.

For SN 2019tsf, our multi-frequency VLA data at  $\delta t = 811$  d–824 d after the first ATLAS observation sample the optically thick part of the SED, and are best fitted with a power-law spectrum  $F_\nu \propto \nu^\alpha$  with index  $\alpha = 1.03 \pm 0.05$ , suggesting that  $\nu_{\text{sa}}$  is above the spectral regime of our observations, or  $\nu_{\text{sa}} \gtrsim 21$  GHz. Similarly,  $F_{\text{pk}} \gtrsim 564$   $\mu\text{Jy}$ . These parameters imply a radius of the emitting region  $R \lesssim 10^{15}$  cm, which is difficult to reconcile with the forward shock radius of a SN at  $\delta t > 800$  d after explosion (for which we would expect  $\sim 10^{17}$  cm).

Possible explanations fall into two broad categories, both sharing the requirement that the emitting region is *not* a spher-

<sup>1</sup>IRAF was distributed by the National Optical Astronomy Observatory, which was managed by the Association of Universities for Research in Astronomy (AURA) under a cooperative agreement with the National Science Foundation



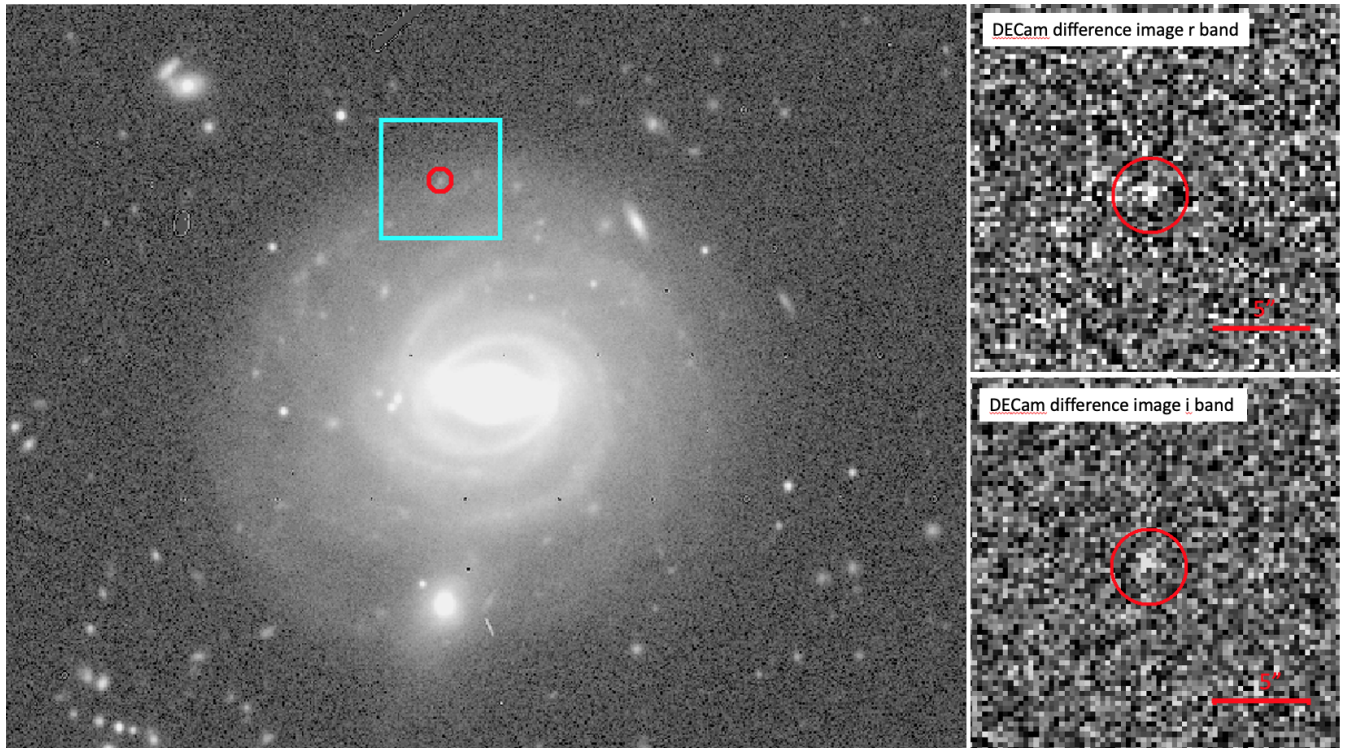


**Figure 1.** The left panel shows the DECam *i*-band image taken on UT 2022-01-12 of SN 2019tsf in M100 (NGC 3541) at phase +322 days. The position of SN 2019tsf is marked with a red circle (2" radius). The right top and bottom panels show the difference images of that same date in *r*- and *i*-band, respectively. The size of the difference image cut outs is indicated in the left panel with a cyan box. The SN is clearly detected in the *i*-band difference image (S/N 5), and marginally in the *r* band.

ically symmetric forward shock launched at the time of explosion. The first possibility is that the radio emitting region consists of a localized overdense “knot” of CSM (as it was proposed for SN 1986J, e.g., Bietenholz & Bartel 2017a,b), or, alternatively, a disk of material in the environment. The second possibility includes the emergence of radiation from a newly-formed compact object, for example in the form of a pulsar wind nebula (PWN, see review by Slane (2017); Dong & Hallinan (2022)). While we leave a detailed study of the radio emission from SN 2019tsf (and its temporal evolution) to future work, here we note that radio observations are consistent with a disk-like geometry of the CSM that we propose in Sec 3.

#### 4. OPTICAL LIGHT CURVE

In addition to the automated photometry provided by the ZTF, we downloaded additional images ZTF from the NASA/IPAC Infrared Science Archive<sup>2</sup> to recover deflections not reported by the automated pipeline. We find three additional epochs of photometry before the earliest reported ZTF photometry when SN 2019tsf is clearly detected. Magnitudes were estimated by modeling the point-spread function (PSF) of each image using field stars and subtracting the model PSF from the target. The magnitudes were then calibrated to AB

magnitudes from the PS1/3 $\pi$  catalog (Chambers et al. 2016). We then separate the flux of the SN from that of its host galaxy by performing difference imaging using a pre-explosion ZTF template image with HOTPANTS (Becker 2015). These new photometry are listed in Table 3.

In Figure 2 we show the optical light curves of SN 2019tsf, where phase 0 is defined as MJD 58785.53, the date of maximum *r*-band magnitude corresponding to  $m_r = 17.43 \pm 0.04$  mag. We correct all photometry for Galactic extinction using  $A_V = 3.1$  and  $E(B - V) = 0.0546$  mag, according to the dust maps from Schlafly & Finkbeiner (2011) and use the Barbary (2016) implementation of the Cardelli et al. (1989) extinction law to correct the photometry. An additional cosmological K-correction of  $+2.5 \log_{10}(1+z)$  is applied to all the photometry. After applying these corrections we measure an absolute magnitude of  $M_o = -17.51$  mag at *o*-band peak.

We proceed to model the light curves using MOSFiT (Guillochon et al. 2018), a Python code designed to fit the light curves of transients using a variety of power sources with the use of the emcee MCMC package (Foreman-Mackey et al. 2013). We model the light curve with a magnetar central engine to both derive physical parameters and estimate an explosion time, which was missed by the photometry of both ATLAS and ZTF. For a full description of the MOSFiT implementation of the magnetar central engine `s1sn` model, see Nicholl et al. (2017). In our models we use the same model priors as the ones in Nicholl et al. (2017), with the exception

<sup>2</sup> <https://irsa.ipac.caltech.edu/Missions/ztf.html>

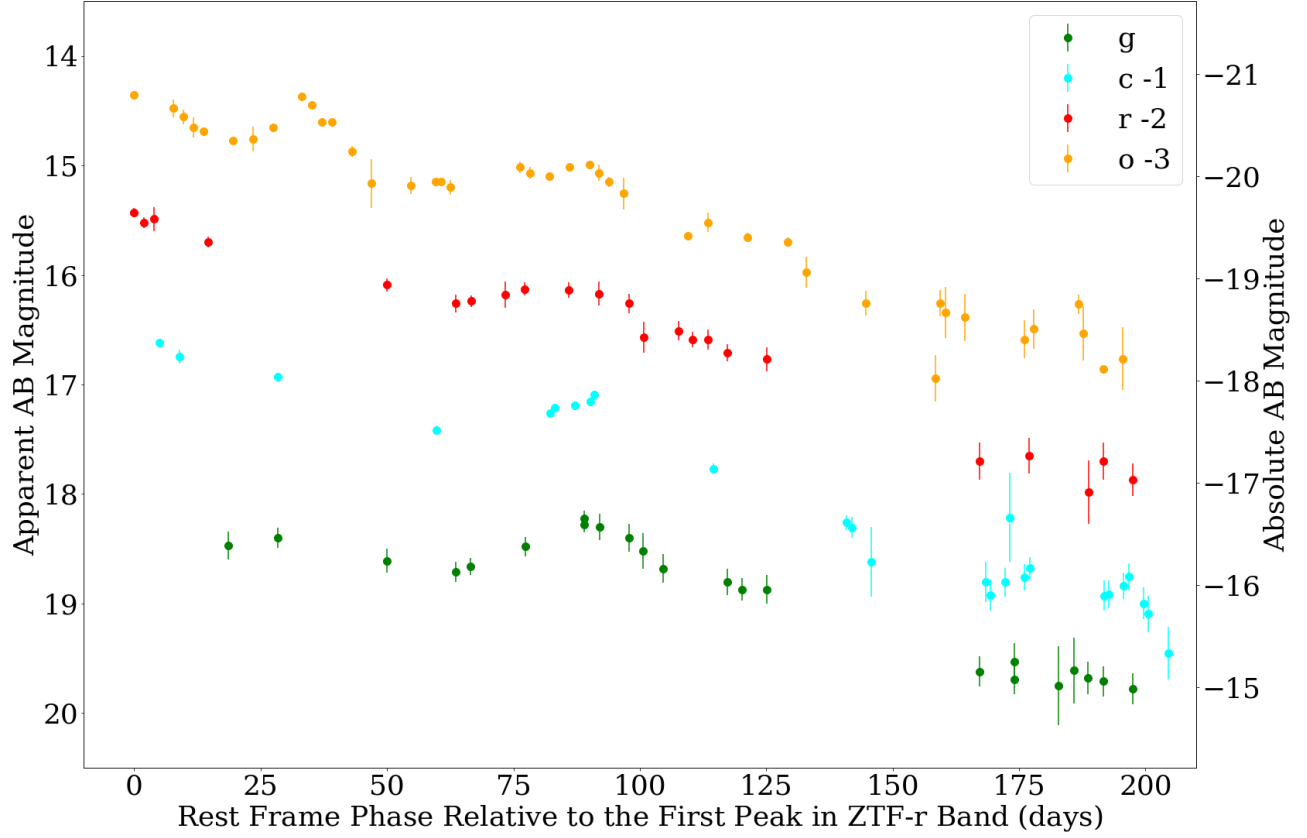


**Figure 2.** Three peaks light curve of SN 2019tsf during the first 200 days after the first ZTF-*r* bands peak ( $t_{\text{peak}_r} = 58785.53$ ). That was also the first detection date in all bands. Light curves in ATLAS-*c* band and ZTF *g* and *r* bands are also included.

**Table 2.** Radio Observations of SN 2019tsf.

Start Date (dd/mm/yy)	Centroid MJD	Phase <sup>a</sup> (d)	Frequency (GHz)	Bandwidth (GHz)	Flux Density <sup>b</sup> ( $\mu\text{Jy}$ )	Facility
Jan 21, 2022	59600.32	811.68	10.0	4	$217 \pm 15$	VLA
Feb 1, 2022	59611.30	822.66	6.2	4	$147 \pm 12$	VLA
Feb 1, 2022	59611.31	822.67	22.0	8	$508 \pm 56$	VLA
Feb 2, 2022	59612.33	823.69	15.0	6	$347 \pm 23$	VLA
Feb 2, 2022	59612.29	823.65	3.0	2	$57 \pm 13$	VLA

NOTE—<sup>a</sup> Days since MJD 58788.64, using the central time of the exposure on source. <sup>b</sup>Uncertainties are quoted at  $1\sigma$ , and upper-limits are quoted at  $3\sigma$ . The reported errors take into account a systematic uncertainty of 10% for data at 22 GHz and 5% for all the other frequencies.

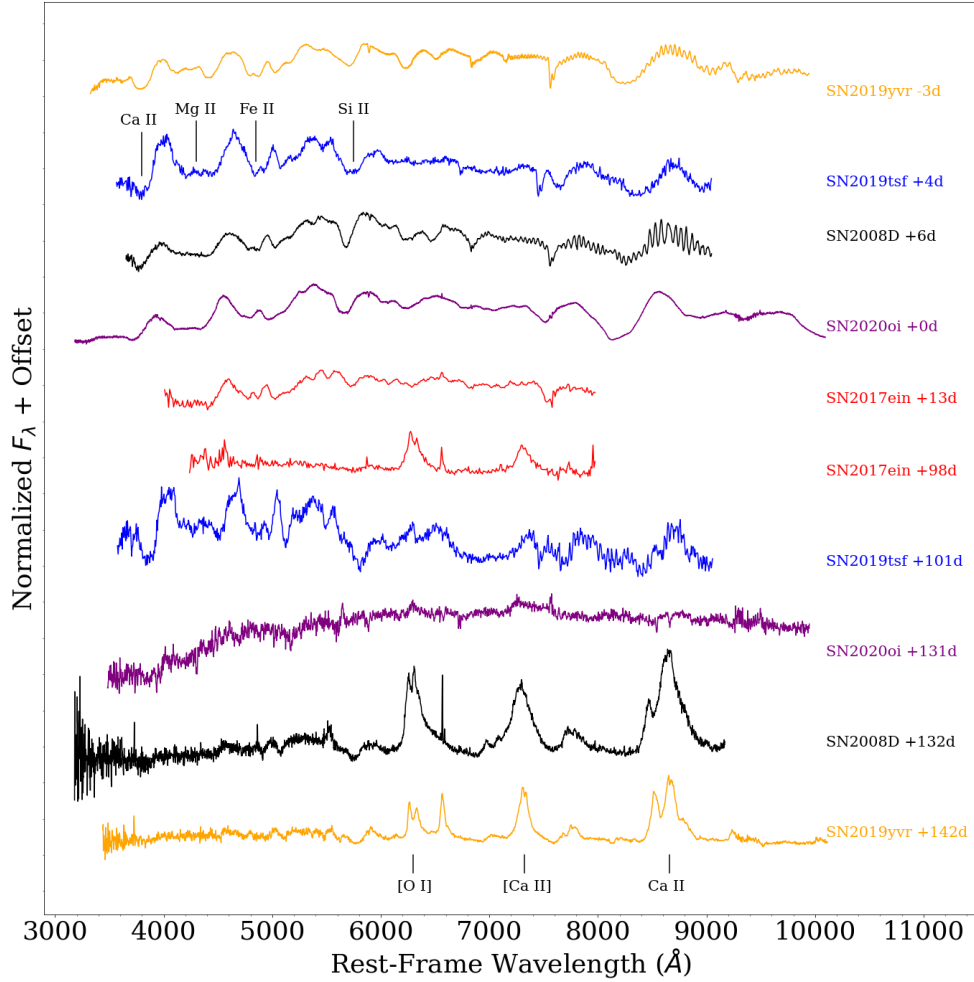


**Figure 3.** The spectra of SN 2019tsf (in blue) taken on +7 and +111 days past the first peak in ZTF- $r$  band from Sollerman et al. (2020). The later spectrum, taken right after the third peak, is still quite similar to the typical Type Ib SNe spectra around peak, and shows slow evolution during this period compared to the spectrum taken on +4 day. Spectra of other SNe Ib/c are included for comparison, including SN Ib 2008D (in black, Malesani et al. (2009); Shivvers et al. (2019)), SN Ib 2019yvr (in orange, Kilpatrick et al. (2021), Auchettl et al in prep.), SN Ic 2020oi (in purple, Gagliano et al. (2022)), SN Ic 2017ein (in red, Teffs et al. (2021)). Phases relative to their peak are marked near the spectra. The early-time spectra of all these SNe Ib/c shows great similarity with the SN 2019tsf, but around  $\sim 100$  days after peak all of them have evolved dramatically.

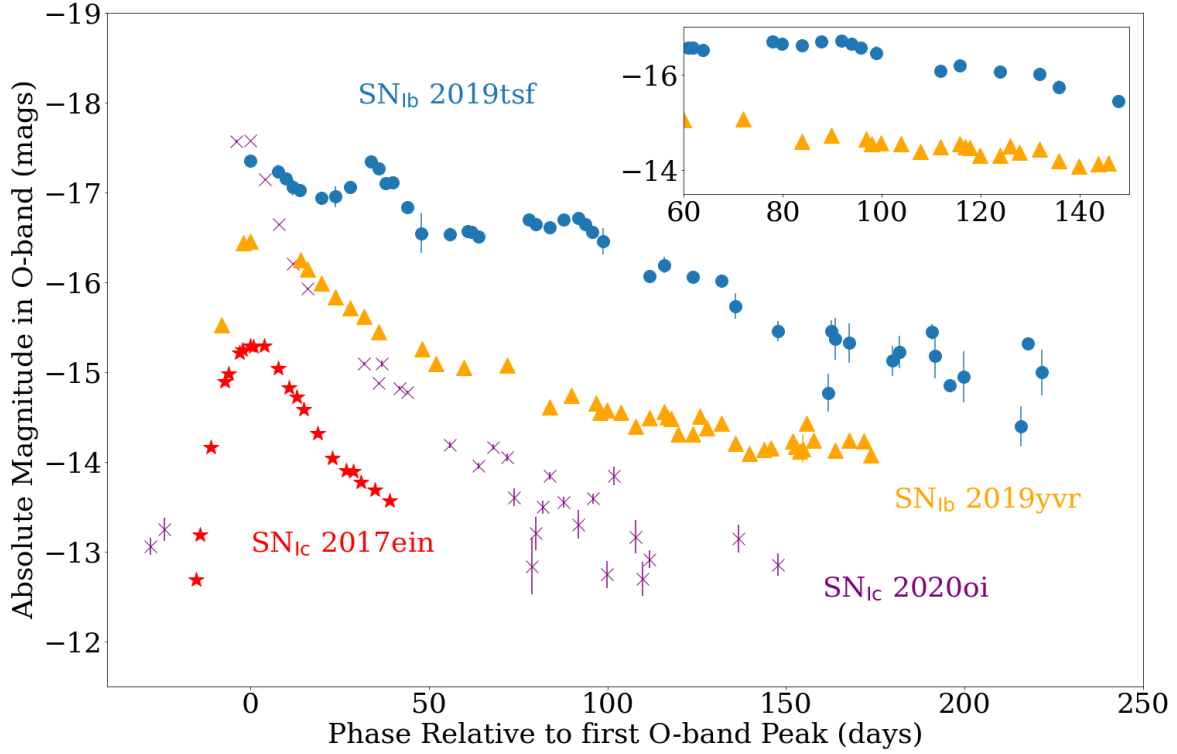


**Figure 4.** Absolute  $o$ -band light curves constructed from the ATLAS sample of SESNe Ib, Ic, IIb. This sample includes only those SNe associated with SNe Ib closest to SN 2019tsf. Yellow triangles designate the Ib SN 2019yvr, blue dots designate the SN 2019tsf, red stars designate the Ic SN 2017ein, and purple cross designate the Ic SN 2020oi. SN 2019tsf behaves differently from the other SESNe, at least until 70 days (relative to the first peak). The late-time evolution, in contrast, bears more similarities to other SNe. The inset plot presents the late-time evolution of two SNe Ib by ATLAS. They clearly have a similar drop rate in luminosity. The  $o$ -band points in the inset have been shifted by  $\sim +1$  mag for both Ib SNe. No other shift has been made in the mag axis for any of the other light curves in the figure.

that we allow for a slower spin period extending to 40 ms to accommodate the lower luminosity of SN 2019tsf, compared to the SLSNe modeled in Nicholl et al. (2017). We run the model using 150 walkers for  $\sim 15,000$  steps and test for convergence by making sure the models reach a potential scale reduction factor  $< 1.3$  (Gelman & Rubin 1992).

The final MOSFiT light curve models are shown in Figure 6 and the posterior distribution of the most relevant parameters are shown in Figure 15. We find a magnetic field  $B = (2.3^{+2.1}_{-0.7}) \times 10^{14}$  G, a spin period of  $p_{\text{spin}} = 22 \pm 3$  ms, an optical opacity  $\kappa = 0.14 \pm 0.05$ , a gamma ray opacity of  $\log(\kappa_{\gamma}/\text{cm}^2\text{g}^{-1}) = -0.54^{+0.21}_{-0.27}$ , an ejecta mass of  $M_{\text{ej}} = 0.86^{+0.67}_{-0.46} M_{\odot}$ , and an ejecta velocity of  $v_{\text{ej}} = 7000 \pm 2600$  km  $\text{s}^{-1}$ . MOSFiT allows us to model the light curve with a simplified one-zone model, and it is therefore unable to

replicate the multi-peak structure of the light curve. Nevertheless, we are able to recover approximate parameters from a model that reproduces the general shape of the light curve. From these models we also measure a total radiated energy of  $E_{\text{rad}} \sim 3 \times 10^{49}$  erg, integrated up to a phase of 250 days.

Additionally, we measure the bolometric luminosity, blackbody radius, and temperature of the SN 2019tsf using the Superbol code (Nicholl 2018). Superbol works by first interpolating the light curves of all individual bands using a polynomial function to account for the times of non-commensal photometry, this way we can fit individual epochs of photometry with a blackbody function. Then, Superbol extrapolates the blackbody function to account for both missing UV and IR flux outside the observed bands. The final bolometric luminosity, radius, and temperature estimated from the photometry are shown in Figure 7. We see the mea-



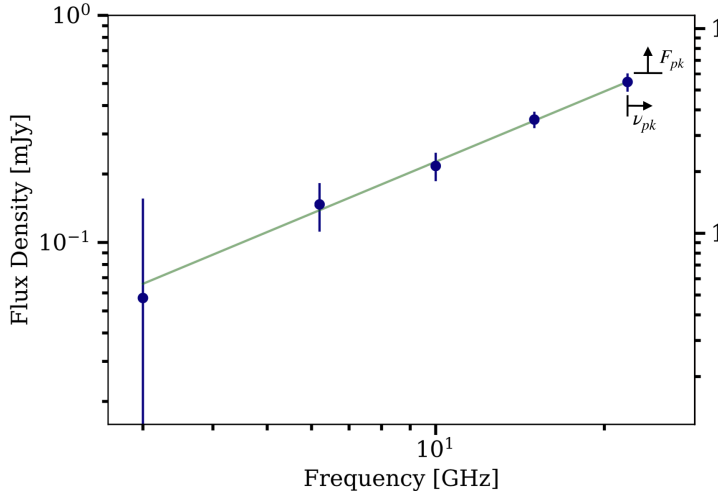


**Figure 5.** VLA observations of SN 2019tsf (navy points). The green line represents a power-law spectrum  $F_\nu \propto \nu^\alpha$  with a best-fitting index  $\alpha = 1.03 \pm 0.05$ . The VLA observations capture only the optically thick portion of the spectrum, suggesting that the peak of the radio SED, that we identify with  $\nu_{\text{sa}}$ , is above the spectral regime of our observations, or  $\nu_{\text{sa}} > 21$  GHz.

**Table 3.** ZTF observations of SN 2019tsf.

MJD	Mag	Filter
58785.53125	$17.43 \pm 0.04$	r
58787.53125	$17.52 \pm 0.05$	r
58789.53515	$17.49 \pm 0.11$	r

NOTE—Optical photometry of ZTF images not reported by the automated pipeline. The magnitudes reported here are the instrumental AB magnitudes without any extinction correction or K-correction applied.

measurements from Superbol match well with the equivalent values measured from the MOSFiT model, with the exception that Superbol estimates a steep rise in temperature after  $\sim 150$  days. It is hard to determine if this rise in temperature is real given that the peak of the blackbody function is well into the UV, and we lack photometry bluer than  $g$ -band, this effect is reflected in the large error bars of those temperature measurements.

## 5. MODELLING THE LIGHT CURVE

ATLAS and ZTF missed the pre-explosion time of the SN 2019tsf and the rise time for the first peak (Taddia et al. 2015; Sollerman et al. 2020). Moreover, the mixing of  $^{56}\text{Ni}$  with the outermost CSM layers would make it hard to confi-

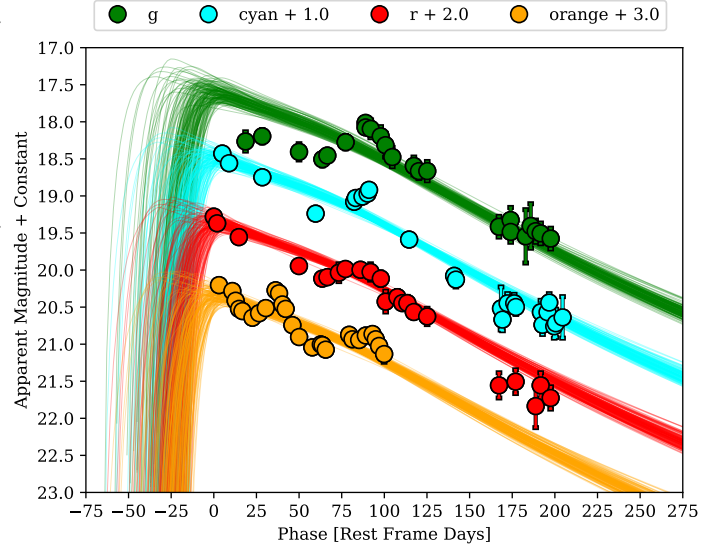


**Figure 6.** Optical light curves of SN 2019tsf modeled with a magnetar central engine model using MOSFiT.

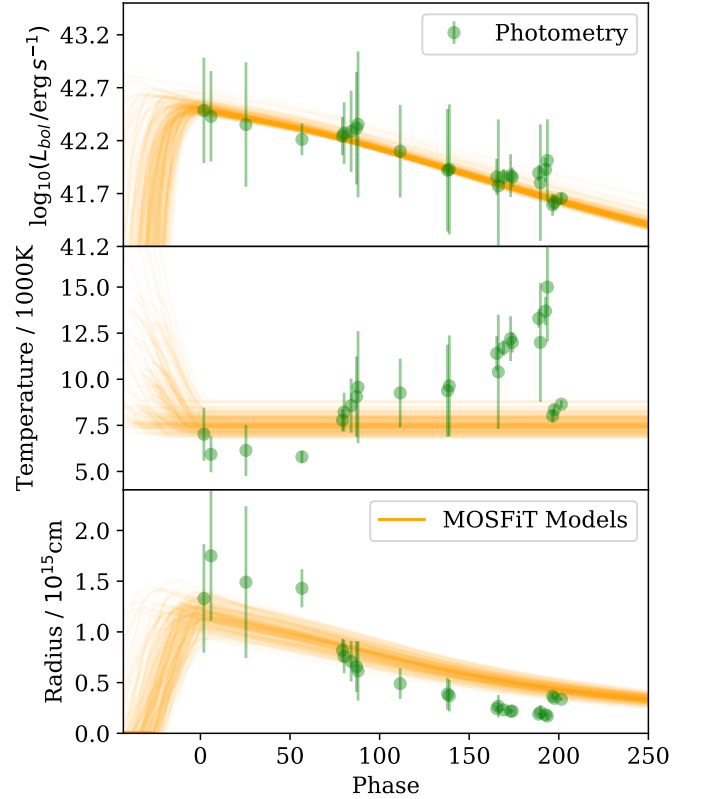


**Figure 7.** Bolometric luminosity (*top*), temperature (*middle*), and radius (*bottom*) evolution of SN 2019tsf. The green points are measurements estimated from the photometry using Superbol, while the orange lines are the equivalent measurements obtained from MOSFiT.

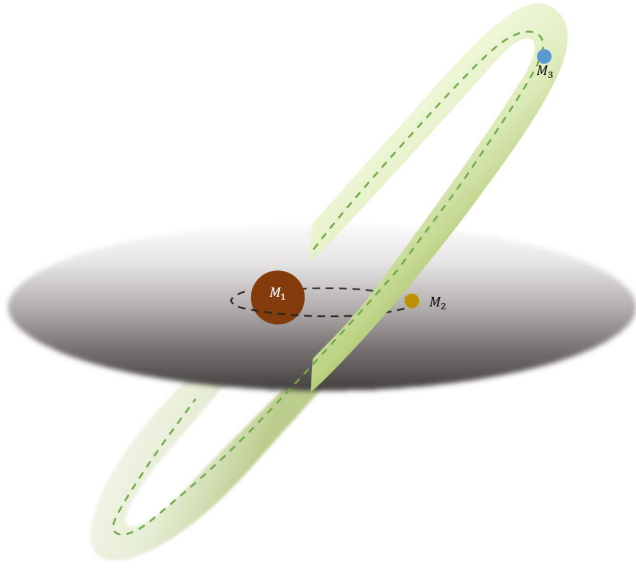


**Figure 8.** Initial condition of the triple system described in Sec. 5.1

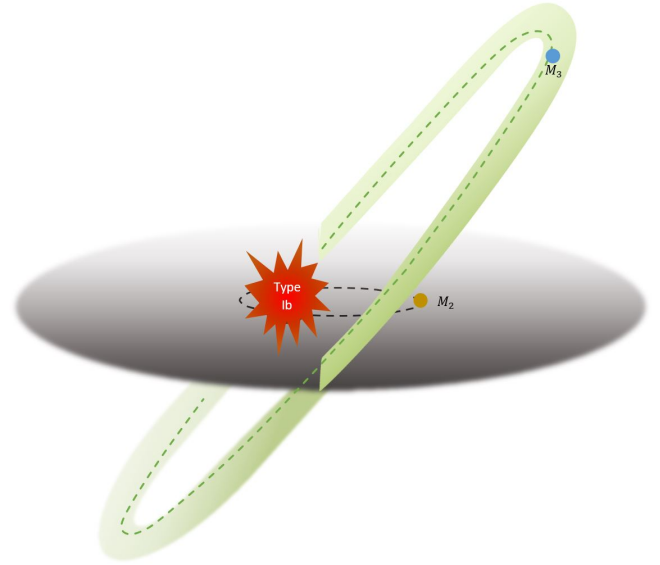
dently rule out the presence of helium lines, one of the key indicators of a Type Ib SN. Because of these properties, modelling and analysing SN 2019tsf is more challenging than for other Type Ib SNe.

In Figure 2, we show the SN 2019tsf light curve, which spans  $\sim 0.5$  to 200 days after the first detection (for later epochs, e.g., +400d since first peak, see Figure 13). In the  $o$ -band, the brightening rise between the first and second peaks is 0.87 mag during the first 50 days. The flux continuously increases by another 0.4 mag during the next 47 days, ten days after the third peak. In this section, we present several progenitor models that can explain our observations of SN 2019tsf. Also, we apply a formalism for a radioactive-decay powered emission to estimate the  $^{56}\text{Ni}$  mass and derive the physical parameters of the explosion.

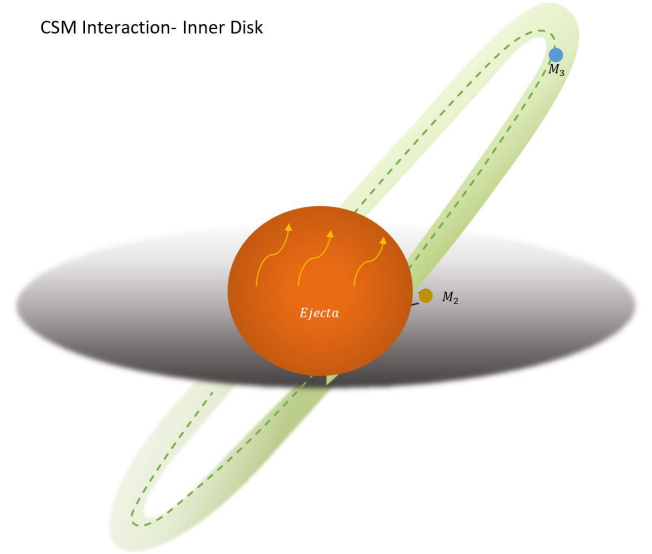
### 5.1. Triple system producing a warped disc

SN 2019tsf is a very rare and possibly unique Type Ib SN. Firstly, as we discuss in Section 6, given that no other Type Ib SN has been observed to have 3 peaks, a 2019tsf-like SN likely happens between once per few 10 and once per few 100 Type Ib SNe. Furthermore, while SN 2019tsf shows no signatures of hydrogen in its spectrum, similarly to typical Type Ib SNe, the significant amount of CSM seen in radio requires an explanation. In this section, we describe a relatively common sequence of events that may happen to Type Ib SN progenitors so that the resulting SN bears similarity to SN 2019tsf.

Firstly, we point out that typical SN Ib progenitors likely had a bound tertiary companion at the moment of explosion, while in the case of SN 2019tsf, the tertiary companion was located relatively close to the SN, as we show in this section. Indeed, the majority of stars more massive than  $8 - 10 M_{\odot}$  are born in binaries or higher-order multiples (Sana et al. 2012b). In particular, more than 30 per cent of such stars are



CSM Interaction- Inner Disk



2<sup>nd</sup> CSM Interaction- Outer Disk

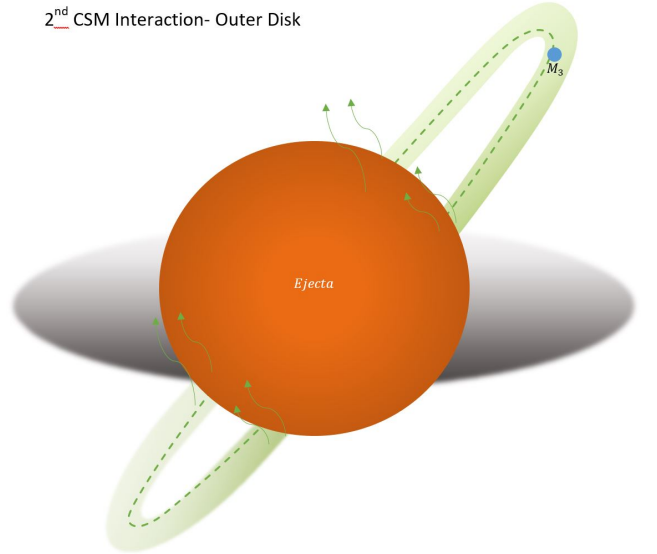


**Figure 9.** The 3 events (from top to bottom) causing the SN peaks in the triple system model described in Sec. 5.1. The SN is observed edge-on to both planes.

triple, and more than 20 per cent are quadruple (Moe & Di Stefano 2017). Therefore every other type Ib supernova progenitor also has a triple and possibly, a quadruple companion. The orbital separations of such companions are log-uniformly spaced from several times the semi-major axis of the inner binary to about  $5 \cdot 10^3$  AU (Moe & Di Stefano 2017). Therefore, for typical Type Ib progenitor separations of 0.1 – 1 AU, the chance of having a triple or quadruple companion located between 10 AU and 100 AU may be estimated to be between  $0.5 \cdot (1/4)$  and  $0.5 \cdot 1/3$ , or about 10 – 15 per cent. Further, we show that a triple companion located at such distances may significantly affect the light curves of Type Ibn SNe.

In this scenario, we assume that SN 2019tsf followed a standard evolutionary path as most type Ib progenitors, in which the primary of initial mass 10 – 25  $M_{\odot}$  was stripped through stable mass transfer by a binary companion of a comparable mass (within a factor 2 – 3 in initial stellar mass compared to the primary), located at separations between 30 – 800  $R_{\odot}$ , see, e.g. Marchant et al. (2021). Binaries with these parameters experience a phase of stable mass transfer after the primary star evolves off the main sequence.

The type Ib supernova then originates from the helium star in a binary with the main sequence companion on a wide orbit. Before it explodes as a supernova, the stripped helium star expands during the shell helium-burning phase, e.g. Hurley et al. (2002), and may overfill its Roche lobe. Therefore, a fraction of type Ib supernovae is expected to undergo mass transfer even at the moment of explosion (Laplace et al. 2020). Normally, type Ib SNe undergoing mass transfer at the moment of explosion would be overfilling their Roche lobe and losing mass through a disc-like outflow and, potentially, a jet (Akashi et al. 2015; Pejcha et al. 2017; Decin et al. 2020). Such supernovae would be observed as SNe Ibn, with the narrow hydrogen lines produced by the disc (although some SNe Ibn may possibly have a different origin). However, when the disc is seen edge-on or when the CSM material is dominantly made of helium, the supernova may be observed as Type Ib since the narrow hydrogen lines will be either obscured by the disc or absent altogether, while narrow helium lines are observationally more challenging to detect. In summary, the mass-transferring SNe scenario may be realised as commonly as SNe Type Ibn (Laplace et al. 2020), and possibly even more commonly if the narrow hydrogen lines are not observed. Further, we assume that SN 2019tsf was a mass-transferring supernova that did not exhibit hydrogen lines, either due to the disc being edge-on or helium-rich.

Finally, as mentioned above, since massive stars are commonly found in higher order multiples (Sana et al. 2012a), it is likely that the progenitor of SN 2019tsf had a tertiary companion. We further assume that SN 2019tsf falls into the 10 – 15 per cent of SNe that have a tertiary companion within 10 – 100 AU. Such situation may occur at a rate of 1 per 7 to 1 per 10 SNe Type Ibn.

From the observations of protostars, the presence of a companion to a star/binary possessing a disc frequently leads to warping of such a disc. We illustrate the suggested formation channel for SN 2019tsf in Fig. 8, 9. In this case, the

supernova interaction with the inner disc generates the first peak, the supernova interaction with the outer disc generates the third peak, and the Nickel decay from the supernova produces the second peak.

Distorted accretion discs are common on various scales, from protoplanetary to AGN discs (e.g. Tremaine & Davis 2014). The disc distortions could range from mild warps/twists to breaks, i.e. two (or more) discs that precess independently. The evolution of warped and broken discs is complicated, and usually, full hydrodynamic simulations are needed to uncover it. Smooth warped discs are governed by the external torques and the inner total angular momentum of the disk, as well as the radial pressure gradient (Miller & Krolik 2013; Sánchez-Salcedo et al. 2018). Breaks in such discs may or may not occur, governed by the viscous and external torque balance. The full range of possible geometries is still uncertain. However, the location of the disc warp could be estimated by comparing the viscous torque to the external one (e.g. Nixon et al. 2013):

$$R_{\text{warp}} \lesssim \left( \frac{1}{4} \mu |\sin 2\theta| (h/r)^{-1} \alpha^{-1} \right)^{1/2} a_{\text{out}} \quad (1)$$

where  $\mu \equiv M_3 / (M_{\text{bin}} + M_3)$  is the reduced mass of the triple,  $\theta$  is the inclination angle of the disc,  $h/r$  is the aspect ratio of the disc,  $\alpha$  is the Shakura-Sunayev parameter and  $a_{\text{out}}$  is the tertiary’s separation. Hence, given the parameters of the disc and its progenitors, the location of the break could be estimated and set constraints on the location and time of the induced SN peak. The break in the disc could then explain the presence of the third peak as the explosion will propagate in this medium.

For the tertiary companions within 10 – 100 AU, the disc warp will occur at comparable separations, leading to the third peak  $t_{3\text{rdpeak}} = R_{\text{break}} / v_{\text{SN,shock}}$  occurring within 30 – 300 d of the SN. For a characteristic disc expansion velocity of about 50 – 100 km/s, as follows from an alpha-disc model with  $\alpha = 0.01$ , the disc material would have to be ejected within a few  $10^4$  d before the SN. Therefore, for typical pre-explosion mass loss rates of  $10^{-3} M_{\odot}/\text{yr}$ , observed in the final decades before core-collapse supernovae (e.g., Brethauer et al. 2022a; Jacobson-Galán et al. 2022), the amount of CSM in the inner disc is  $3 \cdot 10^{-2} - 6 \cdot 10^{-2} M_{\odot}/\text{yr}$ . Using the models from Metzger & Pejcha (2017), we find that the shock interaction of the supernova with the disc will produce the magnitude of the peak in agreement with the observations. The subsequent, later interaction of the CSM with the outer disc material requires a disc overdensity to be present to be consistent with the light curve.

In summary, the warped disc model predicts the timings of the peaks similar to those in SN 2019tsf. The scenario is expected to occur approximately ten times more rarely than SNe Ibn, and the magnitudes of the peaks are qualitatively consistent with the uncertain pre-supernova evolution models of massive stars.

## 5.2. Magnetar model + Radioactive decay

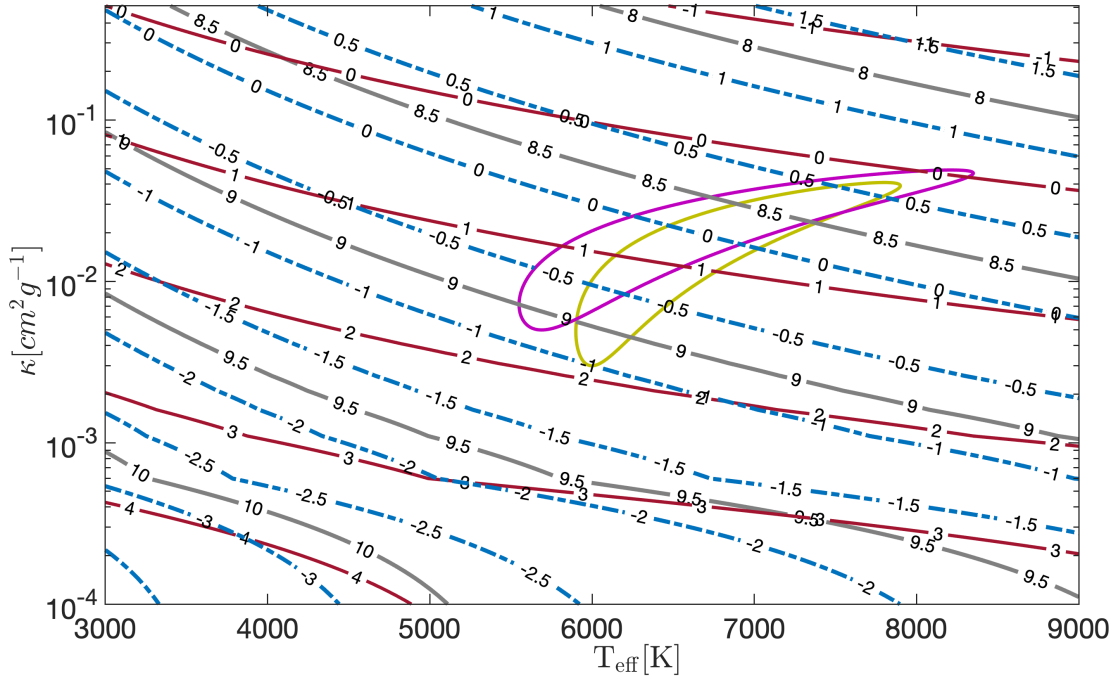


**Figure 10.** Map of ejecta temperature  $T$  versus optical opacity  $\kappa_i$  overlaid with contours of the magnetar surface field strength  $\log_{10}(B_{\text{NS}}/10^{14}\text{G})$  (red solid lines) and supernova ejecta mass  $\log_{10}(M_{\text{ej}})$  (blue dashed lines), for assumed magnetar spin period  $P_0 = 3$  ms (chosen post-hoc because it gives values  $M_{\text{ej}} \sim 1 - 7 M_{\odot}$  in accordance with progenitor expectations as ejecta mass, velocity, etc.). The gray dash line is the ejecta velocity ( $0.005 - 0.04c$ , speed of light) derive from the condition  $t_{\text{pk}} \lesssim t_{\text{sd}}$ . The purple and yellow ellipses are the  $1\sigma$  contours for  $L_{\text{pk}}$  and  $t_{\text{pk}}$  based on the multi SE SN 2019tsf light curve data. The opacity range we find agrees with that found by Kleiser & Kasen (2014) for hydrogen-deficient ejecta in this temperature range  $T \rightarrow T_{\text{eff}}$ .

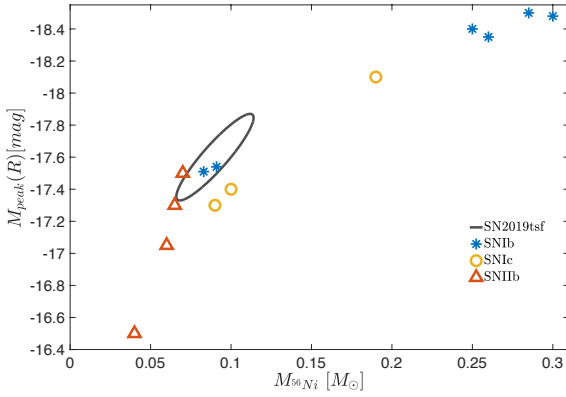


**Figure 11.** The  $^{56}\text{Ni}$  mass of SN 2019tsf following equations 9 and 12 compared to typical SESN those of SN Ib, Ic, and I Ib (Ben-Ami et al. 2014; Dessart et al. 2016).

An alternative mechanism for powering the light curves of SESNe is via sustained energy injection from a central compact object formed during the explosion. One often discussed possibility is a rapidly-spinning neutron star (NS) with a strong surface dipole magnetic field  $B_{\text{NS}} \sim 10^{13} - 10^{15} \text{G}$ , which spins down and releases its rotational energy in the form of a magnetized wind on a timescale of days to years (Ostriker & Gunn 1971; Kasen & Bildsten 2010; Woosley 2010). This wind inflates behind the supernova ejecta a compact magnetized nebula of charged particles (e.g., Metzger et al. 2014) that powers the optical emission through thermalization by the ejecta of the high-energy synchrotron and inverse-Compton radiation released by these particles (Vurm & Metzger 2021). Though mainly considered as a model for Type I SLSNe (e.g., Margutti et al. 2017; Nicholl et al. 2017; Moriya et al. 2022), magnetar engines have been invoked to boost the luminosities of other types of SN or SN-like transients (e.g., Yu et al. 2013; Sukhbold & Thompson 2017;



Prentice et al. 2018; Gomez et al. 2019). Models for SN light curves have also been proposed that invoke a combination of a magnetar engine, ejecta-CSM interaction, and  $^{56}\text{Ni}$  decay (e.g., Chatzopoulos et al. 2013; Chen et al. 2022).

The rotation energy of a NS born with a rotational period  $P = 2\pi/\Omega$  and angular velocity  $\Omega$  can be written  $E_{\text{rot}} = I_{\text{NS}}\Omega^2/2$ , where  $I_{\text{NS}} \approx 1.6 \times 10^{45} \text{ g cm}^2$  is the moment of inertia of a  $1.4M_{\odot}$  NS (Lattimer & Schutz 2005). The magnetar loses rotational energy according to

$$-\frac{dE_{\text{rot}}}{dt} = I_{\text{NS}}\Omega\dot{\Omega} = L_{\text{sd}}, \quad (2)$$

where the dipole spin-down luminosity can be written (Contopoulos et al. 1999; Metzger et al. 2015)

$$L_{\text{sd}} = \frac{B_{\text{NS}}^2 R_{\text{NS}}^6 \Omega^4}{c^3}, \quad (3)$$

and  $R_{\text{NS}} \approx 12 \text{ km}$  is the NS radius. The solution to Eq. (2) is given by

$$L_{\text{sd}} = -\frac{dE_{\text{rot}}}{dt} = \frac{E_{\text{rot},0}}{t_{\text{sd}}} \left(1 + \frac{t}{t_{\text{sd}}}\right)^{-2}, \quad (4)$$

where the characteristic dipole spin-down time is

$$t_{\text{sd}} = \frac{E_{\text{rot},0}}{L_{\text{sd},0}} = \frac{6c^3 I_{\text{NS}}}{B_{\text{NS}}^2 \Omega_0^2 R_{\text{NS}}^6}, \quad (5)$$

and the subscript ‘0’ denotes evaluation at  $t = 0$ .

Optical radiation escapes, and the supernova light curve peaks, on the radiative diffusion timescale (e.g., Kasen & Bildsten 2010),

$$t_{\text{pk}} \sim t_{\text{d}} \sim \left(\frac{3\kappa_i M_{\text{ej}}}{4\pi v_{\text{ej}} t}\right)^{1/2}, \quad (6)$$

where  $M_{\text{ej}}$  and  $v_{\text{ej}}$  are the mass and mean velocity of the SN ejecta and  $\kappa_i$  is the optical Rosseland mean opacity. Insofar that  $t_{\text{d}} \gtrsim t_{\text{sd}}$ , a large portion of the magnetar’s rotational energy  $E_{\text{rot},0}$  can be transferred to the supernova ejecta and in this limit we have

$$\frac{1}{2} M_{\text{ej}} v_{\text{ej}}^2 \simeq E_{\text{rot},0} \quad (7)$$

The Rosseland mean opacity  $\kappa_i$  depends on the composition and interior temperature  $T$  of the ejecta following (Kleiser & Kasen 2014, see their Fig. 3). The photosphere temperature at  $t_{\text{pk}}$  can be written,

$$T_{\text{eff}} = \left(\frac{L_{\text{pk}}}{4\pi\sigma R_{\text{pk}}^2}\right)^{1/4} \quad (8)$$

where  $R_{\text{pk}} = v_{\text{ej}} t_{\text{pk}}$ .

Combining the above equations, we can use the observed properties of the first  $\{L_{\text{pk}} \sim 2.5 \pm 0.1 \times 10^{42} \text{ erg s}^{-1}, t_{\text{pk}} \sim 0\text{d}\}$  and second light curve peaks  $\{L_{\text{pk}} \sim 7 \pm 0.08 \times$

$10^{42} \text{ erg s}^{-1}, t_{\text{pk}} \sim 50\text{d}\}$  to create contours of  $B_{\text{NS}}$  and  $M_{\text{ej}}$  in the space of  $T_{\text{eff}}$  and  $\kappa_i$ , as shown in Fig. 10. Here we assume  $P_0 = 3 \text{ ms}$ . We see that the first/second peak can be explained by a magnetic field of  $B = \{5, 70\} \times 10^{13} \text{ G}$  and  $M_{\text{ej}} = \{0.75, 7.6\} M_{\odot}$  respectively. We further see that the  $\kappa_i(T)$  in the range of our solutions agree with those for Herich ejecta found by (Kleiser & Kasen 2014, their Fig. 3). In figure 6 we include those values to fit the light curve with magnetar engine by using MOSFIT.

The magnetar engine can potentially explain the first peak in the light curve of SN 2019tsf and after  $\sim 40$  days, the second peak is the radioactive heating; after  $\sim 40$ -50 days, the third peak could be explained by weak CSM interaction. As known, the opacity of SN ejecta is strongly dependent on its ionization state and temperature. In Figure 10, we showed within the temperature – opacity phase plot a function of the ejecta SN (blue dash line) and magnetic field contours (dark red solid line). The ellipse shows the zone lies of the SESN SN 2019tsf first and second peaks. The maximum SN 2019tsf ejecta mass could have  $M_{\text{ej}} = 2.63 M_{\odot}$ ,  $B_{\text{NS}} = 3.54 \times 10^{14} \text{ G}$  with  $\kappa = 0.04 \text{ cm}^2 \text{ g}^{-1}$ ,  $T \sim 8300 \text{ K}$  constrain with (Kleiser & Kasen 2014) Figure 3. Nevertheless, those values of the SN 2019tsf first and second peaks are not noticeable for Ib SN as a magnetar engine. Accordingly, we conclude that the SN 2019tsf first peak is best explained with a predominant magnetar engine without any contribution of the radioactive heating or the CSM interaction.

Assuming that the second post-peak photometry is caused directly from radioactive decay, the decay rate  $\sim 0.0104 \text{ mag day}^{-1}$  (see Figure 2 (a)) must be slower or close to the  $^{56}\text{Co}$  decline  $\sim 0.01 \text{ mag day}^{-1}$ . The photometry after the third peak declines by 200 days with rate of  $\sim 0.0182 \text{ mag day}^{-1}$  occurs more rapidly than the  $^{56}\text{Co}$  decay rate. This rate, therefore, can’t be consistent with  $^{56}\text{Co}$  decay. Therefore, the second peak (yellow ellipse in figure 10) with the values lie in the regime of the Ib SN as a magnetar engine with contribution from radioactive heating as the second peak. One of the possibilities to explain the third peak is an unusually CSM interaction with asymmetric geometry (see 5.4). These three processes could explain the three photometric peaks of SN 2019tsf.

### 5.3. Radioactive Decay + Ni mass Model

In this section, we describe the components of a purely radioactive decay powered model and apply it to the light curve of SN 2019tsf at  $\sim 200$  days. Our ATLAS data of SN 2019tsf had a *c/o*-band decline over the first 105 days relative to first with a clear three peaks rate of 1.4 mag. The ATLAS *c*-band is a low resolution observation in this event; the *c*-band is blue, and therefore only used in dark time (Tonry et al. 2016, 2018b). The ATLAS SN 2019tsf bands light curve third peak at  $90 \pm 1.5 \text{ day}$  lie at  $M_{\text{peakIII}} = 18AB$  mag and declines again as a normal SESN Ib over the next 200 days.

Following Arnett (1982) we estimate the  $^{56}\text{Ni}$  mass at the time of maximum light, where we assume that 100% of the SN light is caused by radioactive decay within the

expanding ejecta. In the context of SN Ia correlation between the observed luminosity at the maximum light to the  $^{56}\text{Ni}$  see (Stritzinger et al. 2006).  $\frac{M_{56\text{Ni}}}{M_{\odot}} \sim \frac{L_{\text{max}}[\text{erg s}^{-1}]}{2 \times 10^{43}}$ . Mostly the energy deposition in the ejecta of a SN Ia, IIb/pec is solely due to the rate of the radioactive decay chain  $^{56}\text{Ni} \xrightarrow{t_{\text{decay}} = 8.77 \text{ d}} ^{56}\text{Co} \xrightarrow{t_{\text{decay}} = 111.3 \text{ d}} ^{56}\text{Fe}$  (Arnett 1982; Stritzinger et al. 2006; Gagliano et al. 2022).  $\gamma$ -rays released in this process are then thermalized in the expanding SN ejecta and, for phases  $t \gtrsim 60$  days after explosion,  $^{56}\text{Co}$  beta-decay will power the bolometric light curve until the decays of other radioactive species such as  $^{57}\text{Co}$  and  $^{55}\text{Fe}$  become dominant (e.g.,  $t \gtrsim 50$  days after explosion; red dot-dashed line in Fig. 14).

Recent work by (Khatami & Kasen 2019) present an accurate analytic modeling of the ejecta properties at the time of peak luminosity, this is a model derived empirically from simulations. For the decay chain consisting of  $^{56}\text{Ni} \longrightarrow ^{56}\text{Co} \longrightarrow ^{56}\text{Fe}$ , the  $^{56}\text{Ni}$  mass is given by

$$M_{\text{Ni}56} = \frac{L_{\text{peak}} \beta^2 t_{\text{peak}}^2}{2 \varepsilon_{\text{Ni}} t_{\text{Ni}}^2} \left( \left( 1 - \frac{\varepsilon_{\text{Co}}}{\varepsilon_{\text{Ni}}} \right) \times \right. \\ \left. (1 - (1 + \beta t_{\text{peak}}/t_{\text{Ni}}) e^{-\beta t_{\text{peak}}/t_{\text{Ni}}}) + \right. \\ \left. \frac{\varepsilon_{\text{Co}} t_{\text{Co}}^2}{\varepsilon_{\text{Ni}} t_{\text{Ni}}^2} \left( 1 - (1 + \beta t_{\text{peak}}/t_{\text{Co}}) e^{-\beta t_{\text{peak}}/t_{\text{Co}}} \right) \right)^{-1} \quad (9)$$

where  $t_{\text{Ni}} = 8.77$  days,  $t_{\text{Co}} = 111.3$  days is the timescale for the radioactive decay of  $^{56}\text{Ni}$  into  $^{56}\text{Co}$  and  $^{56}\text{Co}$  into  $^{56}\text{Fe}$ , and  $\varepsilon_{\text{Ni}} = 3.9 \times 10^{10} \text{ erg g}^{-1} \text{ s}^{-1}$  and  $\varepsilon_{\text{Co}} = 6.8 \times 10^9 \text{ erg g}^{-1} \text{ s}^{-1}$  are the specific heating rates (the amount of energy per unit mass released) from these decays (in solar mass units:  $\varepsilon_{\text{Ni}} = 6.45 \times 10^{43} \text{ erg s}^{-1} M_{\odot}^{-1}$  and  $\varepsilon_{\text{Co}} = 1.45 \times 10^{43} \text{ erg s}^{-1} M_{\odot}^{-1}$ ). We adopt a value of  $\beta = 0.9$ , suitable for SNe Ic (Gagliano et al. 2022). The diffusion timescale  $t_d$  can be calculated from the rise time  $t_s$  by numerically solving the equation

$$\frac{t_{\text{peak}}}{t_d} = 0.11 \ln \left( 1 + \frac{9t_s}{t_d} \right) + 0.36, \quad (10)$$

and, from the diffusion timescale  $t_d = \left( \frac{3\kappa M_{\text{ej}}}{4\pi v_{\text{ej}} c \zeta} \right)^{0.5}$ ,  $\zeta$  is the specifies the energy density gradient at the ejecta surface. We adopt the same constant value as (Khatami & Kasen 2019)  $\zeta = \pi^2/3$  the total ejecta mass is then found by

$$M_{\text{ej}} = t_d^2 v_{\text{ej}} \frac{c}{\kappa}, \quad (11)$$

(Dessart et al. 2015, 2016) show a simple polynomial fit of the SESN (Ib, IIb, Ic) bolometric luminosity in maximum R-band magnitude as a function of  $^{56}\text{Ni}$  mass.

$$M_{\text{peak}}(R) [\text{mag}] = -16.21 - 16.44 M_{56\text{Ni}} + 29.93 M_{56\text{Ni}}^2, \quad (12)$$

Where the  $^{56}\text{Ni}$  mass in solar mass. We adopt the ZTF r-band of SN 2019tsf for the left hand of the equitation.

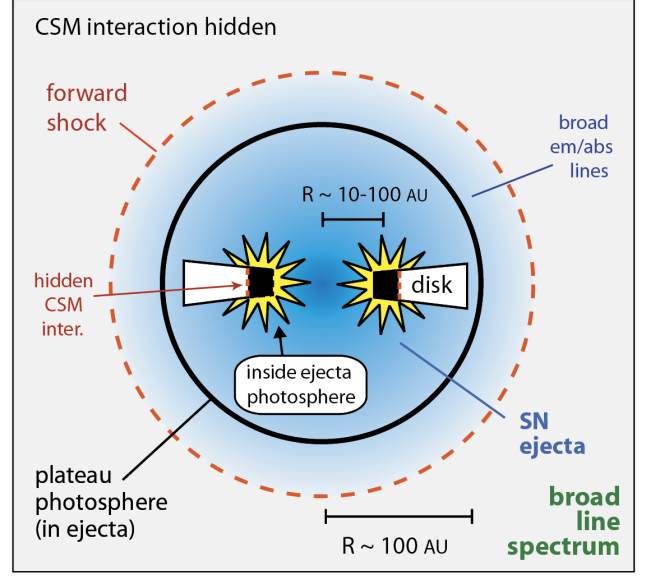


**Figure 12.** A sketch showing how CSM interaction with a compact disc can power the luminosity even if CSM interaction signatures (narrow lines, X-rays, etc.) are not observed. This is adapted from essentially the same sketch shown for the Type II event PTF11iqb by Smith et al. (2015), and then also adopted for the peculiar SN II event iPTF14hls by Andrews & Smith (2018). The model for SN 2019tsf may be nearly identical, except that the SN ejecta are H depleted, making the emergent spectrum a Type Ib, and the radial density distribution of the inner CSM disc may be somewhat different. A key point is that the expanding SN ejecta engulf the compact disc, so while the radiation from this CSM interaction (represented by yellow spikes) can reheat and ionize the ejecta and continue to power the light curve as long as the disc lasts, the radiation is trapped inside the optically thick SN ejecta and is thermalized before it can escape to be seen by an external observer. Thus, an observer sees only broad lines from the fast SN ejecta photosphere. The resulting light curve may appear bumpy if the radial density structure in the disc is not uniform. See Section 5.4 for further discussion.

We determine the total  $^{56}\text{Ni}$  mass following the equations 9 and 12 as shown in Fig. 11. The higher  $^{56}\text{Ni}$  mass is  $0.12 M_{\odot}$  and the lower value  $0.065 M_{\odot}$ . In fact, the results validate the facts we know about the overlap and similarities between the two types Ib and IIb SN. The ellipse lies between SNe IIb and includes two typical SNe Ib.

#### 5.4. SN ejecta running into disc

In normal SESNe, the ejected envelope can only stay opaque as long as heating from radioactive decay can keep it ionized; since radioactivity decays exponentially, the ejected envelope quickly expands, cools, and recombines, then becomes neutral and transitions to the late nebular phase. The main peak of the light curve can only last as long as it takes for the heat to diffuse out, which lasts a month or so depending on the ejecta mass. Interacting SNe (Smith 2017) can potentially sustain a high luminosity for much longer times, since the luminosity generated by CSM interaction can re-

main high as long as there is dense CSM for the ejecta to crash into. Normally we see narrow H or He lines from the slow CSM that is ahead of the shock and photoionized by the shock itself. However, there are thought to be cases where the CSM interaction may be strong, but where the normal signatures of CSM like narrow lines and X-rays may be hidden from view. One way to hide the CSM interaction signatures is if the dense CSM resides in a compact (10s of AU) and asymmetric geometry (Smith et al. 2015), such as a disc that may arise from pre-SN binary interaction (Smith & Arnett 2014). In Section 5.1 we discussed one idea for how such a disc may arise, but given the observed diversity of CSM mass, radial structure, and geometry seen in interacting SNe (Smith 2017), there must be a variety of ways to produce such a CSM disc (Smith & Arnett 2014). A similar CSM geometry for the type Ib SN2014C showed late-time interaction with H-rich CSM (Brethauer et al. 2022b; Thomas et al. 2022).

Smith et al. (2015) proposed a scenario intended to explain the event PTF11iqb, wherein the expanding SN ejecta expand above and below the equator and completely engulf the disc, but where strong CSM interaction in the equatorial plane continues deep inside the SN ejecta photosphere. Andrews & Smith (2018) adapted this model to explain the extraordinary case of iPTF14hls, with multiple peaks over hundreds of days proposed to occur because of density peaks in the disc. Figure 12 shows the basic idea of this scenario. In this scenario, there is strong CSM interaction in a dense equatorial disc that continues to supply luminosity to the SN even after radioactivity fades away. Above and below the equatorial plane, the SN ejecta expand unimpeded, and they engulf the disc. An essential point, however, is that the radiation generated by CSM interaction (yellow spikes in Fig. 12) still produces a high luminosity, but it is buried inside the SN ejecta envelope and cannot escape. Instead of escaping to be observed as narrow emission lines or X-rays, this CSM interaction radiation becomes thermalized and continues to keep the SN ejecta ionized and opaque. Eventually this luminosity diffuses out through the ejecta, but when it does, it has the characteristics of a normal SN ejecta photosphere. In fact, this additional CSM interaction luminosity that gets thermalized within the SN ejecta has the effect of prolonging the optically thick SN photosphere phase and delaying the onset of a normal nebular phase. The duration of this phase depends on the radial extent and mass of the CSM disc, rather than the exponential decay of radioactivity, and the luminosity may rise and fall as higher and lower density regions of the disc are encountered by the shock. Eventually, the disc will be obliterated and the luminosity will drop, or the CSM interaction may continue but the optical depth will eventually drop at larger radii, at which time it may resemble a SN IIn with visible signs of CSM interaction being revealed. In both cases of PTF11iqb and PTF14hls, late time spectra after the bright optical thick phase ended did indeed reveal asymmetric narrow lines from continued CSM interaction that had likely been present the whole time, but was buried underneath the photosphere. In the case of SN 2019tsf, we unfortunately did

not obtain deep late-time spectra to determine if the CSM interaction continued long enough to be revealed again.

A notable difference between SN 2019tsf and the previously studied cases of PTF11iqb and iPTF14hls is that both previous cases had massive H-rich envelopes and exhibited spectra similar to SNe II-P or II-L during their photospheric phases in contrast to the fast ejecta in SN 2019tsf exhibiting no hydrogen. Interestingly, however, this does not mean that the slow CSM disc of SN 2019tsf must necessarily be H-free. Due to an extended CSM, the photosphere may engulf the shocked regions of the disk, this way hiding the hydrogen. Indeed, the narrow Balmer lines that might be emitted from this disc if it does have a significant H abundance would be thermalized and therefore erased from the spectrum when the CSM interaction luminosity eventually diffuses out of the ejecta see, e.g. Roth et al. (2016). From the point of view of the progenitor's evolution, it would have been very interesting to have obtained deep late-time spectra to determine if any H emission was present in that disc.

A twisted and non-spherical CSM profile would be mostly the result of binary evolution during which the primary fills its Roche lobe; this occurs during an interaction between stellar winds and mass transfer (Yoon et al. 2017). In this binary system, the primary star fills its Roche lobe during the evolving stage, depending on the evolutionary state of the stellar core when this occurs and the initial separation. The mass transfer could happen in more than one phase (Lauterborn 1970; Yoon 2015). If the mass ratio of the stellar components is sufficiently large, the system will experience unstable mass transfer and lead to a common envelope event or binary mergers. In the other case, when the initial mass ratio is mild, the mass transfer is stable the primary will end with a small amount of hydrogen (in the envelope). Such a binary stellar evolution scenario could lead to an SN Ib with a disc surrounding it. As we showed above, the H/He-lines (in the spectra) then can become hidden below the photosphere after that disc is surrounded by the fast SN ejecta (Dessart et al. 2012; Smith et al. 2015; Andrews & Smith 2018). In summary, in this section, we investigated the non-spherically symmetric CSM, the history of the eccentricity binary, the multi-peaked light curve, and the disappearance of H-lines in the spectra in the early time.

## 6. DISCUSSION

### 6.1. Modelling and Caveats

Since our ATLAS bands light curve for SN 2019tsf does not contain the early rising phase of the explosion and only includes two bands (o and c), our modelling fit to the observations is relatively unrestricted. In particular, our results are sensitive to our assumptions about the explosion time and initial conditions for the SN (i.e initial binary system mass, disc expansion velocity, rotational period see 5). However, in our modelling, we preferred realistic initial values for masses, mass loss rates and opacity based on the observations of other SNe Ib. Most such SNe data have properties consistent with the models we use to explain the properties of SN 2019tsf. One such key property is the estimated ejecta

mass ( $M_{\text{ej}} \sim 1.7 - 5.2M_{\odot}$ ) of ordinary SNe Ib (Drout et al. 2011; Dessart et al. 2016), which agrees well with our data.

The biggest modelling challenge is to explain the multiple peaks of the light curve of SN 2019tsf, with its limited bands, jointly with the rare H/He-deficient spectrum. On the other hand, the observational data let us infer the distinct features of the CSM interaction, such as non-spherical geometry and highly asymmetric mass distribution, perhaps in a disc. Such geometries allow the CSM interaction to hide the H/He under the photosphere (Smith et al. 2015; Metzger & Pejcha 2017; Andrews & Smith 2018). Furthermore, the peculiar CSM profile allows for moderate material exchange between the disc and the ejecta (see 5.4). Eventually, the ejecta will expand freely and wholly devour the CSM (Smith et al. 2015). In the context of other core-collapse SNe (e.g. SNe Type IIn), the current understanding is that the CSM interaction may be the most plausible pathway for explaining the protracted, re-brightening or irregular light curves, e.g. Andrews & Smith (2018).

### 6.2. How unique is SN 2019tsf?

The diversity of light curves and spectra of SESNe likely reflects the diversity of the possible outcomes of multiple stellar evolution pathways of massive stars. The SESN progenitor may be stripped through stable mass transfer or common envelope evolution, likely corresponding to SNe Type Ib or SNe Type Ic. The stripped core-helium burning star may produce CSM through wind or pre-supernova eruptions before exploding (Matsumoto & Metzger 2022). At low metallicities, the donor may expand significantly due to stellar evolution when entering the shell-helium burning phase and overflow the Roche lobe (Laplace et al. 2020), as likely happened in SN 2019tsf. Roche lobe overflow necessarily leads to mass ejection (can also be conservative), the geometry of which may be diverse as in the case of low mass stars and may include spherical, jetted and disc-like features (Soker & Livio 1994; Decin et al. 2020). However, at the high mass transfer rates expected from pre-supernova light curves, mass loss is likely to proceed through a disc (Lu et al. 2022). Furthermore, a significant fraction of massive stars is expected to have a tertiary stellar companion (Sana et al. 2012b). The stellar companion may be commonly located within 100 AU of the supernova, potentially affecting the geometry of mass loss such that the effect is observable in the first 100 d of the light curve. Finally, the asymmetric CSM will be observed differently depending on the viewing angle.

While a detailed calculation of the probability of multiple peaks is limited by the uncertainties of multiple massive stellar evolutionary pathways and the scope of this study, we can expect that double-peaked SNe Type Ibn should be relatively common among SNe Type Ib in low-metallicity environments, at least so long as the Laplace et al. (2020) model is correct. Therefore, analysing the distribution of occurrence times of the third peak can provide a tantalising new lens on the tertiary companion properties of massive stars, assuming that many more SNe like SN 2019tsf shall be found. These conclusions are in qualitative agreement with the cur-

rent observations of SNe Type Ib. For example, 224 SNe Type Ib/c are currently listed on the (ZTF) Bright Transient Survey catalogue (Fremming et al. 2020; Perley et al. 2020), likely representative of stably stripped stars. Among these, 20 SNe are Type Ibn, potentially indicative of SNe from stably stripped stars in low-metallicity hosts overflowing their Roche lobe. SN 2019tsf is a unique SN Type Ib, making it about 20 times more rare than SNe Type Ibn and about 200 times rarer than typical SNe Ib did not show multiple peaks. The true occurrence rate of multi-peaked SNe may be a factor of several or more higher, however, since not all the SNe Type Ib in the ZTF survey have been sampled well enough to detect multiple peaks. The best example of such missed SNe is SN 2019tsf itself, which was recognised as a triple-peak SN only thanks to the ATLAS data, it is possible that ZTF SNe have multiple peaks.

### 6.3. Discovering Other Multi-Peaked Supernovae

Understanding unusual multi-peak SESNe requires continuous spectral and photometric monitoring over  $\gtrsim 1000$  d timescale and determining whether there are any signs of interaction with hydrogen/helium-rich/poor CSM. Most observed SNe showing more than one peak are CCSNe and nearly every SN Ia has two peaks in the red/infrared. The SLSNe can also show several-peaked light curves and early/late bumps, although modelling these is beyond our paper (see, Moriya et al. 2022; Chen et al. 2022). These highly luminous transients can be explained by predominantly CSM interactions, manifested in the high explosion energies ( $\gtrsim 10^{51}$  erg) and the relatively low amount of radioactive material.

At the same time, the signatures imprinted in the light curves and spectra provide essential clues about (and should be studied together with) the late-time evolution of binary/triple/multiple massive stars. The different outcomes of such evolution can produce various light or dense CSM, e.g. Andrews & Smith (2018); Gangopadhyay et al. (2022). Several multi-peaked SNe were observed in the last decade without clearly identified progenitors. Moreover, homogeneity and diversity of the light curves and spectra of different classes of multi-peaked SNe are necessary to pinpoint their progenitors. In contrast, SNe Type IIn associated with luminous blue variable (LBV) stars are believed to originate from massive stars, e.g. Smith et al. (2010); Gal-Yam (2017) in a binary system (Foley et al. 2007). All this hints at a critical need for early observations such as pre-supernova progenitor observations and light curve evolution, early rise time, color evolution across various wavelengths, estimates of the mass-loss rate, and the optical thickness of the ejecta, early and late radio observations and other ejecta properties. Such measurements across the different classes of multi-peaked SNe will greatly contribute to removing the uncertainty in their origins (Andrews & Smith 2018; Fang et al. 2022). Finally, for the unknown SESN progenitors, multiple empirical observational relations can be used to infer the ejecta properties such as the ejecta mass or explosion energy of the progeni-



tors (Drout et al. 2011; Dessart et al. 2015, 2016), which all contribute significantly to our understanding of such SNe.

## 7. CONCLUSIONS

In this paper, we have presented a rare SESN Ib type known as SN 2019tsf with 430 days of ATLAS data after explosion. Also, this transient was observed four months after peak with VLA. This kind of transient shows multi-peaks that are hard to connect to a progenitor mechanism. There are a few multi-peaked SNe for different types (see Arcavi et al. 2017). SN 2019tsf shows a second peak 35 days after the first detection. The light curve declines for 45 days until the center of third peak (90 days after first detection). Moreover, no clear spectral signatures of CSM interaction were seen, as discussed in Sollerman et al. (2020). In Figure 4, we compare the SN 2019tsf light curve to some prototypical SNe Ib and Ic such as SN 2019yvr, SN 2017ein, SN 2020oi respectively, and we conclude that the SN 2019tsf light curve behaves like a SN Ib. Nevertheless, we estimate the  $^{56}\text{Ni}$  mass by following (Dessart et al. 2011, 2015; Khatami & Kasen 2019; Gagliano et al. 2022) and find that it could be powered by  $0.07 - 0.12 M_{\odot}$  (see fig. 11). Additionally, we explore the possibility that the entire light curve is powered by a magnetar and find a best fit of a magnetar of magnetic field  $B \sim 2 \times 10^{14}$  G and spin period  $P_{\text{spin}} \sim 22$  ms, and an ejecta mass of  $M_{\text{ej}} \sim 0.9 M_{\odot}$ . In figure 3 we show the SN 2019tsf spectra at 7 and 111 days. In the early spectra we find evidence of Ca II, Mg II, Fe II, and Si II features similar to typical, early Ib SNe SN2008D, 2019yvr. SN 2019tsf hardly evolves in later phase even until  $\geq 100$  days after peak, and there is no sign of other dominant lines ([O I] 6300, [Ca II] 7326 and Ca II 8662) in SNe Ib/c around same phase, neither does any Hydrogen features. SESN can lack dominant H/He emission lines or even hide them completely (e.g. Matheson et al. 2001; Dessart et al. 2011)). Andrews & Smith (2018) explained the fact that such a CSM interaction did not reveal itself in the spectral evolution due to a particular geometry hiding the interaction site, although actual modeling of such a mechanism remain unexplored. The SN 2019tsf  $^{56}\text{Ni}$  mass estimates in section 5.3 are inadequately broad assumption in the  $M_{\text{peak}}$  R-band of sample Ib (Dessart et al. 2015, 2016). Nonetheless, the  $^{56}\text{Ni}$  mass of SN 2019tsf lies in the typical Ib SN range.

We present alongside our optical data the first epoch of our radio VLA observations (Table 2). As only the optically thick spectrum of the SED can be constrained, we are only able to speculate (estimates radius, mass, velocity etc) that there is a sufficiently dense CSM (either a clump or disc) located at  $R < 10^{15}$  cm from the explosion. Ongoing radio observations and analysis will be published in future work.

We have considered several physical scenarios to explain the multi-peaks SESN SN 2019tsf. These include (i) SN ejecta interaction with a warped disc, (ii) SN ejecta interaction with an asymmetric disc-like CSM formed by binary interaction, (iii) a purely magnetar dominated model, and (iv)

the magnetar model with CSM interaction 5.2. including a warped disc, binary interaction and an asymmetric CSM, which show the ejecta running into disc 5.4, a purely magnetar dominated model, and the magnetar model with CSM interaction 5.2; we trifle favor this model. The ejecta running into disc scenario could also potentially be explained by the asymmetric CSM properties intrinsic to the type-Ib explosion; where the H-lines are hidden during the early evolution. The extraordinary model here is the warped disc scenario as we emphasis the stellar evolution in 5.1. The results of this SESN SN 2019tsf highlight how necessary the early-time observations are for understanding the nature of SN progenitors.

## 8. ACKNOWLEDGEMENTS

The author thanks Kevin Schlaufman and Arshia Maria Jacob for helpful discussions. A.B. acknowledges support for this project from the European Union’s Horizon 2020 research and innovation program under grant agreement No. 865932-ERC-SNeX. MR acknowledges the generous support of Azrieli fellowship. The UCSC team is supported in part by NASA grant 80NSSC20K0953; NSF grant AST-1815935; the Gordon & Betty Moore Foundation; the Heising-Simons Foundation; and by a fellowship from the David and Lucile Packard Foundation to R.J.F. This work has made use of data from the Asteroid Terrestrial- impact Last Alert System (ATLAS) project and the Young Supernova Experiment (YSE; Jones et al. (2021)). The Asteroid Terrestrial- impact Last Alert System (ATLAS) project is primarily funded to search for near earth asteroids through NASA grants NN12AR55G, 80NSSC18K0284, and 80NSSC18K1575; byproducts of the NEO search include images and catalogs from the survey area. The ATLAS science products have been made possible through the contributions of the University of Hawaii Institute for Astronomy, the Queen’s University Belfast, the Space Telescope Science Institute, the South African Astronomical Observatory, and The Millennium Institute of Astrophysics (MAS), Chile. This work was partially funded by Kepler/K2 grant J1944/80NSSC19K0112 and HST GO-15889, and STFC grants ST/T000198/1 and ST/S006109/1. This research is also based on data obtained from the Astro Data Archive at NSF’s NOIRLab. These data are associated with observing program(s) 2020A-0415 (PI A. Rest), 2021A-0275 (PI A. Rest), and 2021B-0325 (PI A. Rest). NOIRLab is managed by the Association of Universities for Research in Astronomy (AURA) under a cooperative agreement with the National Science Foundation. Raw imaging data were processed with the DECam Community Pipeline (Valdes et al. (2014), ASPC, 485, 379). We further acknowledge that the National Radio Astronomy Observatory is a facility of the National Science Foundation operated under cooperative agreement by Associated Universities, Inc.

*Facilities:* DECam, VLA

*Software:* Astropy (Astropy Collaboration et al. 2018), MOSFiT (Guillochon et al. 2018), and NumPy (Harris et al. 2020)

## REFERENCES

- Akashi, M., Sabach, E., Yogev, O., & Soker, N. 2015, *MNRAS*, 453, 2115, doi: [10.1093/mnras/stv1666](https://doi.org/10.1093/mnras/stv1666)
- Anderson, J. P. 2019, *A&A*, 628, A7, doi: [10.1051/0004-6361/201935027](https://doi.org/10.1051/0004-6361/201935027)
- Andrews, J. E., & Smith, N. 2018, *MNRAS*, 477, 74, doi: [10.1093/mnras/sty584](https://doi.org/10.1093/mnras/sty584)
- Arcavi, I., Gal-Yam, A., Yaron, O., et al. 2011, *ApJL*, 742, L18, doi: [10.1088/2041-8205/742/2/L18](https://doi.org/10.1088/2041-8205/742/2/L18)
- Arcavi, I., Hosseinzadeh, G., Brown, P. J., et al. 2017, *ApJL*, 837, L2, doi: [10.3847/2041-8213/aa5be1](https://doi.org/10.3847/2041-8213/aa5be1)
- Arnett, W. D. 1982, *ApJ*, 253, 785, doi: [10.1086/159681](https://doi.org/10.1086/159681)
- Astropy Collaboration, Price-Whelan, A. M., Sipőcz, B. M., et al. 2018, *AJ*, 156, 123, doi: [10.3847/1538-3881/aabc4f](https://doi.org/10.3847/1538-3881/aabc4f)
- Barbary, K. 2016, extinction, v0.3.0, Zenodo, doi: [10.5281/zenodo.804967](https://doi.org/10.5281/zenodo.804967)
- Becker, A. 2015, HOTPANTS: High Order Transform of PSF AND Template Subtraction. <http://ascl.net/1504.004>
- Ben-Ami, S., Gal-Yam, A., Mazzali, P. A., et al. 2014, *ApJ*, 785, 37, doi: [10.1088/0004-637X/785/1/37](https://doi.org/10.1088/0004-637X/785/1/37)
- Bersten, M. C., Folatelli, G., García, F., et al. 2018, *Nature*, 554, 497, doi: [10.1038/nature25151](https://doi.org/10.1038/nature25151)
- Bietenholz, M. F., & Bartel, N. 2017a, *ApJ*, 839, 10, doi: [10.3847/1538-4357/aa67a0](https://doi.org/10.3847/1538-4357/aa67a0)
- . 2017b, *ApJ*, 851, 7, doi: [10.3847/1538-4357/aa960b](https://doi.org/10.3847/1538-4357/aa960b)
- Brethauer, D., Margutti, R., Milisavljevic, D., et al. 2022a, arXiv e-prints, arXiv:2206.00842. <https://arxiv.org/abs/2206.00842>
- . 2022b, arXiv e-prints, arXiv:2206.00842. <https://arxiv.org/abs/2206.00842>
- Buzzoni, B., Delabre, B., Dekker, H., et al. 1984, *The Messenger*, 38, 9
- Cardelli, J. A., Clayton, G. C., & Mathis, J. S. 1989, in *Interstellar Dust*, ed. L. J. Allamandola & A. G. G. M. Tielens, Vol. 135, 5–10
- Chambers, K. C., Magnier, E. A., Metcalfe, N., et al. 2016, arXiv e-prints, arXiv:1612.05560. <https://arxiv.org/abs/1612.05560>
- Chatzopoulos, E., Wheeler, J. C., Vinko, J., Horvath, Z. L., & Nagy, A. 2013, *ApJ*, 773, 76, doi: [10.1088/0004-637X/773/1/76](https://doi.org/10.1088/0004-637X/773/1/76)
- Chen, Z. H., Yan, L., Kangas, T., et al. 2022, arXiv e-prints, arXiv:2202.02060. <https://arxiv.org/abs/2202.02060>
- Chevalier, R. A. 1982, *ApJ*, 258, 790, doi: [10.1086/160126](https://doi.org/10.1086/160126)
- . 1998, *ApJ*, 499, 810, doi: [10.1086/305676](https://doi.org/10.1086/305676)
- Chevalier, R. A., & Fransson, C. 2017, *Thermal and Non-thermal Emission from Circumstellar Interaction*, ed. A. W. Alsabti & P. Murdin, 875, doi: [10.1007/978-3-319-21846-5\\_34](https://doi.org/10.1007/978-3-319-21846-5_34)
- Chomiuk, L., Chornock, R., Soderberg, A. M., et al. 2011, *ApJ*, 743, 114, doi: [10.1088/0004-637X/743/2/114](https://doi.org/10.1088/0004-637X/743/2/114)
- Claeys, J. S. W., de Mink, S. E., Pols, O. R., Eldridge, J. J., & Baes, M. 2011, *A&A*, 528, A131, doi: [10.1051/0004-6361/201015410](https://doi.org/10.1051/0004-6361/201015410)
- Contopoulos, I., Kazanas, D., & Fendt, C. 1999, *ApJ*, 511, 351, doi: [10.1086/306652](https://doi.org/10.1086/306652)
- Decin, L., Montargès, M., Richards, A. M. S., et al. 2020, *Science*, 369, 1497, doi: [10.1126/science.abb1229](https://doi.org/10.1126/science.abb1229)
- DeMarchi, L., Margutti, R., Dittman, J., et al. 2022, arXiv e-prints, arXiv:2203.07388. <https://arxiv.org/abs/2203.07388>
- Dessart, L., Hillier, D. J., Li, C., & Woosley, S. 2012, *MNRAS*, 424, 2139, doi: [10.1111/j.1365-2966.2012.21374.x](https://doi.org/10.1111/j.1365-2966.2012.21374.x)
- Dessart, L., Hillier, D. J., Livne, E., et al. 2011, *MNRAS*, 414, 2985, doi: [10.1111/j.1365-2966.2011.18598.x](https://doi.org/10.1111/j.1365-2966.2011.18598.x)
- Dessart, L., Hillier, D. J., Woosley, S., et al. 2015, *MNRAS*, 453, 2189, doi: [10.1093/mnras/stv1747](https://doi.org/10.1093/mnras/stv1747)
- . 2016, *MNRAS*, 458, 1618, doi: [10.1093/mnras/stw418](https://doi.org/10.1093/mnras/stw418)
- Dessart, L., Yoon, S.-C., Aguilera-Dena, D. R., & Langer, N. 2020, *A&A*, 642, A106, doi: [10.1051/0004-6361/202038763](https://doi.org/10.1051/0004-6361/202038763)
- Dong, D., & Hallinan, G. 2022, arXiv e-prints, arXiv:2206.11911. <https://arxiv.org/abs/2206.11911>
- Drout, M. R., Soderberg, A. M., Gal-Yam, A., et al. 2011, *ApJ*, 741, 97, doi: [10.1088/0004-637X/741/2/97](https://doi.org/10.1088/0004-637X/741/2/97)
- Ertl, T., Woosley, S. E., Sukhbold, T., & Janka, H. T. 2019, arXiv e-prints, arXiv:1910.01641. <https://arxiv.org/abs/1910.01641>
- Fang, Q., Maeda, K., Kuncarayakti, H., et al. 2022, *ApJ*, 928, 151, doi: [10.3847/1538-4357/ac4f60](https://doi.org/10.3847/1538-4357/ac4f60)
- Foley, R. J., Smith, N., Ganeshalingam, M., et al. 2007, *ApJL*, 657, L105, doi: [10.1086/513145](https://doi.org/10.1086/513145)
- Foreman-Mackey, D. 2016, *The Journal of Open Source Software*, 1, doi: [10.21105/joss.00024](https://doi.org/10.21105/joss.00024)
- Foreman-Mackey, D., Hogg, D. W., Lang, D., & Goodman, J. 2013, *PASP*, 125, 306, doi: [10.1086/670067](https://doi.org/10.1086/670067)
- Fox, O. D., Van Dyk, S. D., Williams, B. F., et al. 2022, *ApJL*, 929, L15, doi: [10.3847/2041-8213/ac5890](https://doi.org/10.3847/2041-8213/ac5890)
- Fremling, C., Miller, A. A., Sharma, Y., et al. 2020, *ApJ*, 895, 32, doi: [10.3847/1538-4357/ab8943](https://doi.org/10.3847/1538-4357/ab8943)
- Gagliano, A., Izzo, L., Kilpatrick, C. D., et al. 2022, *ApJ*, 924, 55, doi: [10.3847/1538-4357/ac35ec](https://doi.org/10.3847/1538-4357/ac35ec)
- Gal-Yam, A. 2017, *Observational and Physical Classification of Supernovae*, ed. A. W. Alsabti & P. Murdin, 195, doi: [10.1007/978-3-319-21846-5\\_35](https://doi.org/10.1007/978-3-319-21846-5_35)
- Gal-Yam, A., Bruch, R., Schulze, S., et al. 2022, *Nature*, 601, 201, doi: [10.1038/s41586-021-04155-1](https://doi.org/10.1038/s41586-021-04155-1)
- Gangopadhyay, A., Misra, K., Hosseinzadeh, G., et al. 2022, arXiv e-prints, arXiv:2203.15194. <https://arxiv.org/abs/2203.15194>
- Gelman, A., & Rubin, D. B. 1992, *Statistical Science*, 7, 457, doi: [10.1214/ss/1177011136](https://doi.org/10.1214/ss/1177011136)
- Georgy, C., Meynet, G., Walder, R., Folini, D., & Maeder, A. 2009, *A&A*, 502, 611, doi: [10.1051/0004-6361/200811339](https://doi.org/10.1051/0004-6361/200811339)
- Gomez, S., Berger, E., Hosseinzadeh, G., et al. 2021, *ApJ*, 913, 143, doi: [10.3847/1538-4357/abf5e3](https://doi.org/10.3847/1538-4357/abf5e3)

- Gomez, S., Berger, E., Nicholl, M., et al. 2019, *ApJ*, 881, 87, doi: [10.3847/1538-4357/ab2f92](https://doi.org/10.3847/1538-4357/ab2f92)
- Guillochon, J., Nicholl, M., Villar, V. A., et al. 2018, *ApJS*, 236, 6, doi: [10.3847/1538-4365/aab761](https://doi.org/10.3847/1538-4365/aab761)
- Harris, C. R., Millman, K. J., van der Walt, S. J., et al. 2020, *Nature*, 585, 357–362, doi: [10.1038/s41586-020-2649-2](https://doi.org/10.1038/s41586-020-2649-2)
- Hosseinzadeh, G., McCully, C., Zabludoff, A. I., et al. 2019, *ApJL*, 871, L9, doi: [10.3847/2041-8213/aafc61](https://doi.org/10.3847/2041-8213/aafc61)
- Hurley, J. R., Tout, C. A., & Pols, O. R. 2002, *MNRAS*, 329, 897, doi: [10.1046/j.1365-8711.2002.05038.x](https://doi.org/10.1046/j.1365-8711.2002.05038.x)
- Iwamoto, K., Brachwitz, F., Nomoto, K., et al. 1999, *ApJS*, 125, 439, doi: [10.1086/313278](https://doi.org/10.1086/313278)
- Jacobson-Galán, W. V., Dessart, L., Jones, D. O., et al. 2022, *ApJ*, 924, 15, doi: [10.3847/1538-4357/ac3f3a](https://doi.org/10.3847/1538-4357/ac3f3a)
- Janssens, S., Shenar, T., Mahy, L., et al. 2021, *A&A*, 646, A33, doi: [10.1051/0004-6361/202039305](https://doi.org/10.1051/0004-6361/202039305)
- Jones, D. O., Foley, R. J., Narayan, G., et al. 2021, *ApJ*, 908, 143, doi: [10.3847/1538-4357/abd7f5](https://doi.org/10.3847/1538-4357/abd7f5)
- Kasen, D. 2017, in *Handbook of Supernovae*, ed. A. W. Alsabti & P. Murdin, 939, doi: [10.1007/978-3-319-21846-5\\_32](https://doi.org/10.1007/978-3-319-21846-5_32)
- Kasen, D., & Bildsten, L. 2010, *ApJ*, 717, 245, doi: [10.1088/0004-637X/717/1/245](https://doi.org/10.1088/0004-637X/717/1/245)
- Khatami, D. K., & Kasen, D. N. 2019, *ApJ*, 878, 56, doi: [10.3847/1538-4357/ab1f09](https://doi.org/10.3847/1538-4357/ab1f09)
- Kilpatrick, C. D., Drout, M. R., Auchettl, K., et al. 2021, *MNRAS*, 504, 2073, doi: [10.1093/mnras/stab838](https://doi.org/10.1093/mnras/stab838)
- Kleiser, I. K. W., & Kasen, D. 2014, *MNRAS*, 438, 318, doi: [10.1093/mnras/stt2191](https://doi.org/10.1093/mnras/stt2191)
- Laplace, E., Göteborg, Y., de Mink, S. E., Justham, S., & Farmer, R. 2020, *A&A*, 637, A6, doi: [10.1051/0004-6361/201937300](https://doi.org/10.1051/0004-6361/201937300)
- Lattimer, J. M., & Schutz, B. F. 2005, *ApJ*, 629, 979, doi: [10.1086/431543](https://doi.org/10.1086/431543)
- Lauterborn, D. 1970, *A&A*, 7, 150
- Lee, K. H., Bartos, I., Cook, A., et al. 2022, arXiv e-prints, arXiv:2202.09739. <https://arxiv.org/abs/2202.09739>
- Leung, S.-C., Fuller, J., & Nomoto, K. 2021, *ApJ*, 915, 80, doi: [10.3847/1538-4357/abfcbe](https://doi.org/10.3847/1538-4357/abfcbe)
- Lu, W., Fuller, J., Quataert, E., & Bonnerot, C. 2022, arXiv e-prints, arXiv:2204.00847. <https://arxiv.org/abs/2204.00847>
- MacFadyen, A. I., & Woosley, S. E. 1999, *ApJ*, 524, 262, doi: [10.1086/307790](https://doi.org/10.1086/307790)
- Malesani, D., Fynbo, J. P. U., Hjorth, J., et al. 2009, in *American Institute of Physics Conference Series*, Vol. 1111, *Probing Stellar Populations Out to the Distant Universe: Cefalu 2008*, Proceedings of the International Conference, ed. G. Giobbi, A. Tornambe, G. Raimondo, M. Limongi, L. A. Antonelli, N. Menci, & E. Brocato, 627–628, doi: [10.1063/1.3141622](https://doi.org/10.1063/1.3141622)
- Marchant, P., Pappas, K. M. W., Gallegos-Garcia, M., et al. 2021, *A&A*, 650, A107, doi: [10.1051/0004-6361/202039992](https://doi.org/10.1051/0004-6361/202039992)
- Margutti, R., Metzger, B. D., Chornock, R., et al. 2017, *ApJ*, 836, 25, doi: [10.3847/1538-4357/836/1/25](https://doi.org/10.3847/1538-4357/836/1/25)
- Matheson, T., Filippenko, A. V., Li, W., Leonard, D. C., & Shields, J. C. 2001, *AJ*, 121, 1648, doi: [10.1086/319390](https://doi.org/10.1086/319390)
- Matsumoto, T., & Metzger, B. D. 2022, arXiv e-prints, arXiv:2206.08377. <https://arxiv.org/abs/2206.08377>
- McMullin, J. P., Waters, B., Schiebel, D., Young, W., & Golap, K. 2007, in *Astronomical Society of the Pacific Conference Series*, Vol. 376, *Astronomical Data Analysis Software and Systems XVI*, ed. R. A. Shaw, F. Hill, & D. J. Bell, 127
- Metzger, B. D. 2022, arXiv e-prints, arXiv:2203.04331. <https://arxiv.org/abs/2203.04331>
- Metzger, B. D., Margalit, B., Kasen, D., & Quataert, E. 2015, *MNRAS*, 454, 3311, doi: [10.1093/mnras/stv2224](https://doi.org/10.1093/mnras/stv2224)
- Metzger, B. D., & Pejcha, O. 2017, *MNRAS*, 471, 3200, doi: [10.1093/mnras/stx1768](https://doi.org/10.1093/mnras/stx1768)
- Metzger, B. D., Vurm, I., Hascöet, R., & Beloborodov, A. M. 2014, *MNRAS*, 437, 703, doi: [10.1093/mnras/stt1922](https://doi.org/10.1093/mnras/stt1922)
- Miller, M. C., & Krolik, J. H. 2013, *ApJ*, 774, 43, doi: [10.1088/0004-637X/774/1/43](https://doi.org/10.1088/0004-637X/774/1/43)
- Modjaz, M., Bianco, F. B., Siwek, M., et al. 2019, arXiv e-prints, arXiv:1901.00872. <https://arxiv.org/abs/1901.00872>
- Moe, M., & Di Stefano, R. 2017, *ApJS*, 230, 15, doi: [10.3847/1538-4365/aa6fb6](https://doi.org/10.3847/1538-4365/aa6fb6)
- Moriya, T. J., Murase, K., Kashiyama, K., & Blinnikov, S. I. 2022, arXiv e-prints, arXiv:2202.03082. <https://arxiv.org/abs/2202.03082>
- Nagataki, S. 2018, *Reports on Progress in Physics*, 81, 026901, doi: [10.1088/1361-6633/aa97a8](https://doi.org/10.1088/1361-6633/aa97a8)
- Nicholl, M. 2018, *Research Notes of the American Astronomical Society*, 2, 230, doi: [10.3847/2515-5172/aaf799](https://doi.org/10.3847/2515-5172/aaf799)
- Nicholl, M., Guillochon, J., & Berger, E. 2017, *ApJ*, 850, 55, doi: [10.3847/1538-4357/aa9334](https://doi.org/10.3847/1538-4357/aa9334)
- Nixon, C., King, A., & Price, D. 2013, *MNRAS*, 434, 1946, doi: [10.1093/mnras/stt1136](https://doi.org/10.1093/mnras/stt1136)
- Ostriker, J. P., & Gunn, J. E. 1971, *ApJL*, 164, L95, doi: [10.1086/180699](https://doi.org/10.1086/180699)
- Pastorello, A., Wang, X. F., Ciabattari, F., et al. 2016, *MNRAS*, 456, 853, doi: [10.1093/mnras/stv2634](https://doi.org/10.1093/mnras/stv2634)
- Pejcha, O., Metzger, B. D., Tyles, J. G., & Tomida, K. 2017, *ApJ*, 850, 59, doi: [10.3847/1538-4357/aa95b9](https://doi.org/10.3847/1538-4357/aa95b9)
- Pellegrino, C., Howell, D. A., Terreran, G., et al. 2022, arXiv e-prints, arXiv:2205.07894. <https://arxiv.org/abs/2205.07894>
- Perley, D. A., Fremling, C., Sollerman, J., et al. 2020, *ApJ*, 904, 35, doi: [10.3847/1538-4357/abbd98](https://doi.org/10.3847/1538-4357/abbd98)
- Perley, D. A., Sollerman, J., Schulze, S., et al. 2022, *ApJ*, 927, 180, doi: [10.3847/1538-4357/ac478e](https://doi.org/10.3847/1538-4357/ac478e)
- Prentice, S. J., & Mazzali, P. A. 2017, *MNRAS*, 469, 2672, doi: [10.1093/mnras/stx980](https://doi.org/10.1093/mnras/stx980)

- Prentice, S. J., Maguire, K., Smartt, S. J., et al. 2018, *ApJL*, 865, L3, doi: [10.3847/2041-8213/aadd90](https://doi.org/10.3847/2041-8213/aadd90)
- Prentice, S. J., Ashall, C., James, P. A., et al. 2019, *MNRAS*, 485, 1559, doi: [10.1093/mnras/sty3399](https://doi.org/10.1093/mnras/sty3399)
- Quimby, R. M., Kulkarni, S. R., Kasliwal, M. M., et al. 2011, *Nature*, 474, 487, doi: [10.1038/nature10095](https://doi.org/10.1038/nature10095)
- Rest, A., Dhawan, S., Mandel, K., et al. 2022, *Transient Name Server AstroNote*, 24, 1
- Riess, A. G., Macri, L. M., Hoffmann, S. L., et al. 2016, *ApJ*, 826, 56, doi: [10.3847/0004-637X/826/1/56](https://doi.org/10.3847/0004-637X/826/1/56)
- Riess, A. G., Casertano, S., Yuan, W., et al. 2018, *ApJ*, 861, 126, doi: [10.3847/1538-4357/aac82e](https://doi.org/10.3847/1538-4357/aac82e)
- Rimoldi, A., Portegies Zwart, S., & Rossi, E. M. 2016, *Computational Astrophysics and Cosmology*, 3, 2, doi: [10.1186/s40668-016-0015-4](https://doi.org/10.1186/s40668-016-0015-4)
- Roth, N., Kasen, D., Guillochon, J., & Ramirez-Ruiz, E. 2016, *ApJ*, 827, 3, doi: [10.3847/0004-637X/827/1/3](https://doi.org/10.3847/0004-637X/827/1/3)
- Roy, R., Sollerman, J., Silverman, J. M., et al. 2016, *A&A*, 596, A67, doi: [10.1051/0004-6361/201527947](https://doi.org/10.1051/0004-6361/201527947)
- Sana, H., de Mink, S. E., de Koter, A., et al. 2012a, *Science*, 337, 444, doi: [10.1126/science.1223344](https://doi.org/10.1126/science.1223344)
- . 2012b, *Science*, 337, 444, doi: [10.1126/science.1223344](https://doi.org/10.1126/science.1223344)
- Sánchez-Salcedo, F. J., Chametla, R. O., & Santillán, A. 2018, *ApJ*, 860, 129, doi: [10.3847/1538-4357/aac494](https://doi.org/10.3847/1538-4357/aac494)
- Schlafly, E. F., & Finkbeiner, D. P. 2011, *ApJ*, 737, 103, doi: [10.1088/0004-637X/737/2/103](https://doi.org/10.1088/0004-637X/737/2/103)
- Schlegel, D. J., Finkbeiner, D. P., & Davis, M. 1998, *ApJ*, 500, 525, doi: [10.1086/305772](https://doi.org/10.1086/305772)
- Shivvers, I., Filippenko, A. V., Silverman, J. M., et al. 2019, *MNRAS*, 482, 1545, doi: [10.1093/mnras/sty2719](https://doi.org/10.1093/mnras/sty2719)
- Slane, P. 2017, *Pulsar Wind Nebulae*, ed. A. W. Alsabti & P. Murdin (Cham: Springer International Publishing), 2159–2179, doi: [10.1007/978-3-319-21846-5\\_95](https://doi.org/10.1007/978-3-319-21846-5_95)
- Smartt, S. J., Valenti, S., Fraser, M., et al. 2015, *A&A*, 579, A40, doi: [10.1051/0004-6361/201425237](https://doi.org/10.1051/0004-6361/201425237)
- Smith, K. W., Smartt, S. J., Young, D. R., et al. 2020, *PASP*, 132, 085002, doi: [10.1088/1538-3873/ab936e](https://doi.org/10.1088/1538-3873/ab936e)
- Smith, N. 2017, *Interacting Supernovae: Types II<sub>n</sub> and Ib<sub>n</sub>*, ed. A. W. Alsabti & P. Murdin, 403, doi: [10.1007/978-3-319-21846-5\\_38](https://doi.org/10.1007/978-3-319-21846-5_38)
- Smith, N., & Arnett, W. D. 2014, *ApJ*, 785, 82, doi: [10.1088/0004-637X/785/2/82](https://doi.org/10.1088/0004-637X/785/2/82)
- Smith, N., Chornock, R., Silverman, J. M., Filippenko, A. V., & Foley, R. J. 2010, *ApJ*, 709, 856, doi: [10.1088/0004-637X/709/2/856](https://doi.org/10.1088/0004-637X/709/2/856)
- Smith, N., Li, W., Filippenko, A. V., & Chornock, R. 2011a, *MNRAS*, 412, 1522, doi: [10.1111/j.1365-2966.2011.17229.x](https://doi.org/10.1111/j.1365-2966.2011.17229.x)
- Smith, N., Li, W., Silverman, J. M., Ganeshalingam, M., & Filippenko, A. V. 2011b, *MNRAS*, 415, 773, doi: [10.1111/j.1365-2966.2011.18763.x](https://doi.org/10.1111/j.1365-2966.2011.18763.x)
- Smith, N., Mauerhan, J. C., Cenko, S. B., et al. 2015, *MNRAS*, 449, 1876, doi: [10.1093/mnras/stv354](https://doi.org/10.1093/mnras/stv354)
- Soker, N., & Livio, M. 1994, *ApJ*, 421, 219, doi: [10.1086/173639](https://doi.org/10.1086/173639)
- Sollerman, J., Fransson, C., Barbarino, C., et al. 2020, *A&A*, 643, A79, doi: [10.1051/0004-6361/202038960](https://doi.org/10.1051/0004-6361/202038960)
- Springob, C. M., Magoulas, C., Colless, M., et al. 2014, *MNRAS*, 445, 2677, doi: [10.1093/mnras/stu1743](https://doi.org/10.1093/mnras/stu1743)
- Stritzinger, M., Leibundgut, B., Walch, S., & Contardo, G. 2006, *A&A*, 450, 241, doi: [10.1051/0004-6361:20053652](https://doi.org/10.1051/0004-6361:20053652)
- Sukhbold, T., & Thompson, T. A. 2017, *MNRAS*, 472, 224, doi: [10.1093/mnras/stx2004](https://doi.org/10.1093/mnras/stx2004)
- Taddia, F., Sollerman, J., Leloudas, G., et al. 2015, *A&A*, 574, A60, doi: [10.1051/0004-6361/201423915](https://doi.org/10.1051/0004-6361/201423915)
- Teffs, J. J., Prentice, S. J., Mazzali, P. A., & Ashall, C. 2021, *MNRAS*, 502, 3829, doi: [10.1093/mnras/stab258](https://doi.org/10.1093/mnras/stab258)
- Thomas, B. P., Wheeler, J. C., Dwarkadas, V. V., et al. 2022, *ApJ*, 930, 57, doi: [10.3847/1538-4357/ac5fa6](https://doi.org/10.3847/1538-4357/ac5fa6)
- Tonry, J., Denneau, L., Stalder, B., et al. 2016, *The Astronomer's Telegram*, 9685
- Tonry, J. L., Denneau, L., Heinze, A. N., et al. 2018a, *Publications of the Astronomical Society of the Pacific*, 130, 064505, doi: [10.1088/1538-3873/aabadf](https://doi.org/10.1088/1538-3873/aabadf)
- Tonry, J. L., Denneau, L., Flewelling, H., et al. 2018b, *ApJ*, 867, 105, doi: [10.3847/1538-4357/aae386](https://doi.org/10.3847/1538-4357/aae386)
- Tramper, F., Straal, S. M., Sanyal, D., et al. 2015, *A&A*, 581, A110, doi: [10.1051/0004-6361/201425390](https://doi.org/10.1051/0004-6361/201425390)
- Tremaine, S., & Davis, S. W. 2014, *MNRAS*, 441, 1408, doi: [10.1093/mnras/stu663](https://doi.org/10.1093/mnras/stu663)
- Valdes, F., Gruendl, R., & DES Project. 2014, in *Astronomical Society of the Pacific Conference Series*, Vol. 485, *Astronomical Data Analysis Software and Systems XXIII*, ed. N. Manset & P. Forshay, 379
- Villar, V. A., Nicholl, M., & Berger, E. 2018, *ApJ*, 869, 166, doi: [10.3847/1538-4357/aaee6a](https://doi.org/10.3847/1538-4357/aaee6a)
- Vurm, I., & Metzger, B. D. 2021, *ApJ*, 917, 77, doi: [10.3847/1538-4357/ac0826](https://doi.org/10.3847/1538-4357/ac0826)
- Wang, Q., Rest, A., Zenati, Y., et al. 2021, *ApJ*, 923, 167, doi: [10.3847/1538-4357/ac2c84](https://doi.org/10.3847/1538-4357/ac2c84)
- Woosley, S. E. 2010, *ApJL*, 719, L204, doi: [10.1088/2041-8205/719/2/L204](https://doi.org/10.1088/2041-8205/719/2/L204)
- Woosley, S. E., & Bloom, J. S. 2006, *ARA&A*, 44, 507, doi: [10.1146/annurev.astro.43.072103.150558](https://doi.org/10.1146/annurev.astro.43.072103.150558)
- Woosley, S. E., Langer, N., & Weaver, T. A. 1993, *ApJ*, 411, 823, doi: [10.1086/172886](https://doi.org/10.1086/172886)
- Yoon, S.-C. 2015, *PASA*, 32, e015, doi: [10.1017/pasa.2015.16](https://doi.org/10.1017/pasa.2015.16)
- Yoon, S.-C., Dessart, L., & Clocchiatti, A. 2017, *ApJ*, 840, 10, doi: [10.3847/1538-4357/aa6afe](https://doi.org/10.3847/1538-4357/aa6afe)
- Yoon, S. C., Woosley, S. E., & Langer, N. 2010, *ApJ*, 725, 940, doi: [10.1088/0004-637X/725/1/940](https://doi.org/10.1088/0004-637X/725/1/940)



Yu, Y.-W., Zhang, B., & Gao, H. 2013, *ApJL*, 776, L40,  
doi: [10.1088/2041-8205/776/2/L40](https://doi.org/10.1088/2041-8205/776/2/L40)

Zenati, Y., Siegel, D. M., Metzger, B. D., & Perets, H. B. 2020,  
*MNRAS*, 499, 4097, doi: [10.1093/mnras/staa3002](https://doi.org/10.1093/mnras/staa3002)

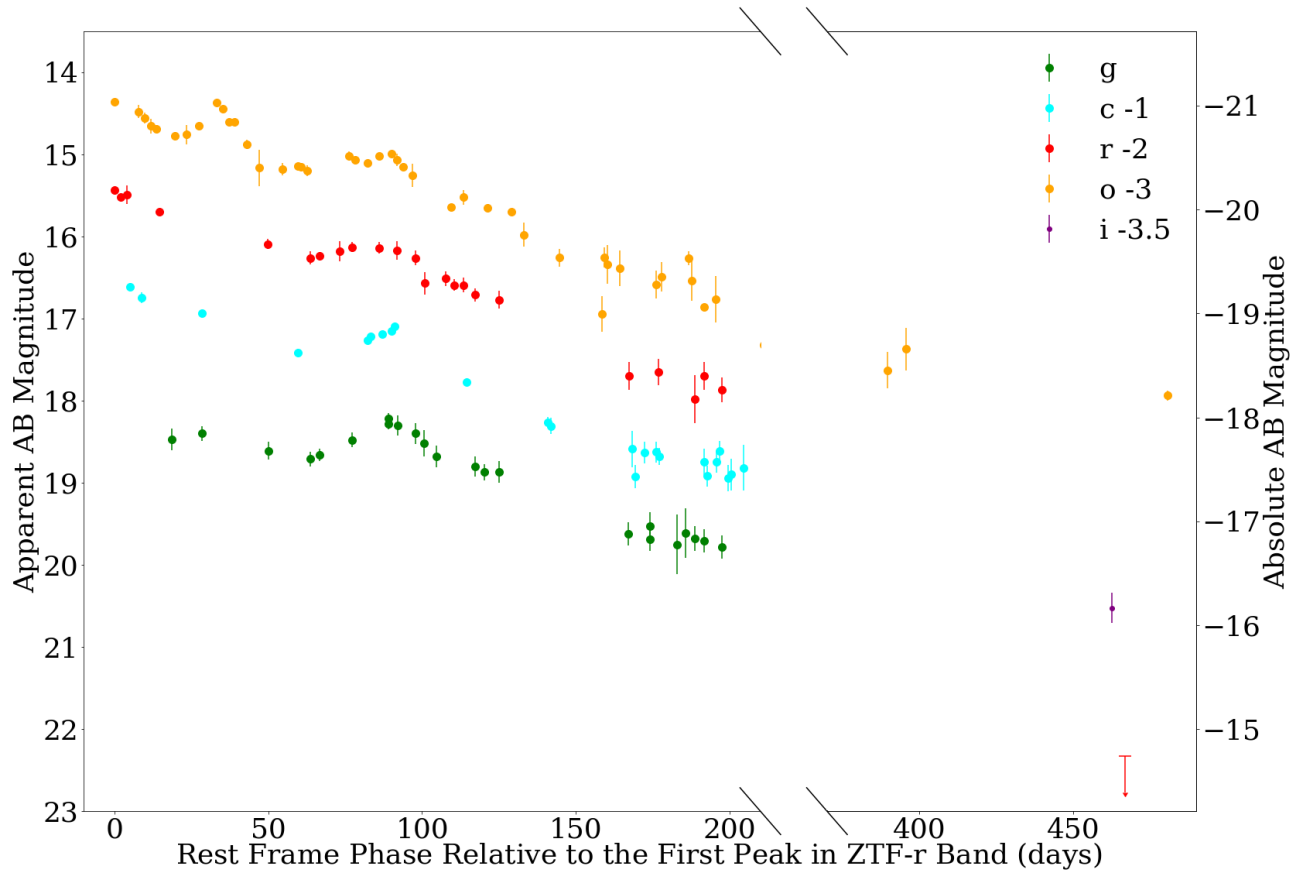


**Figure 13.** The late bands curve evolution during until 433 days relative to the  $t_{peak_r} = 58785.53MJD$ . The SN 2019tsf late data were observed by DECam in the i- and r-band.

#### APPENDIX

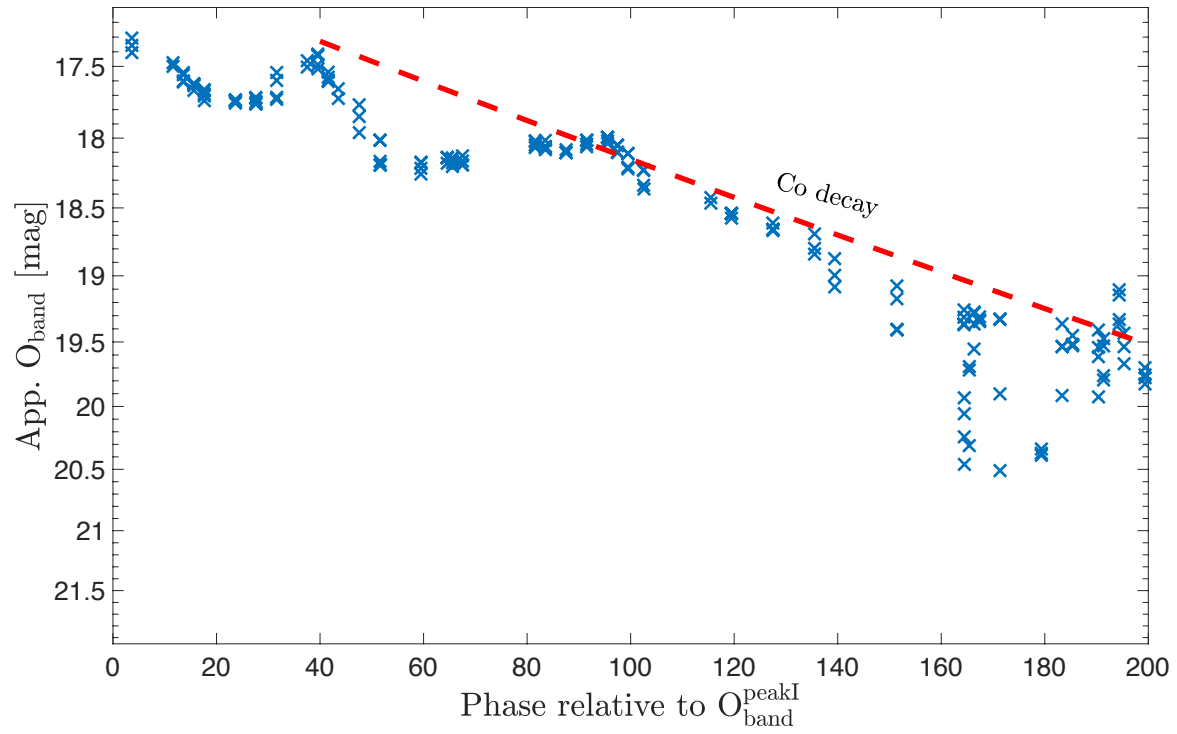


**Figure 14.** The light curve *o*-band evolution during the first 200 days (blue crosses). The expected  $^{56}\text{Co}$  decay rate is shown from second peak (red dashed line). The SN 2019tsf decline is similar to the rate of  $^{56}\text{Co}$  decay.

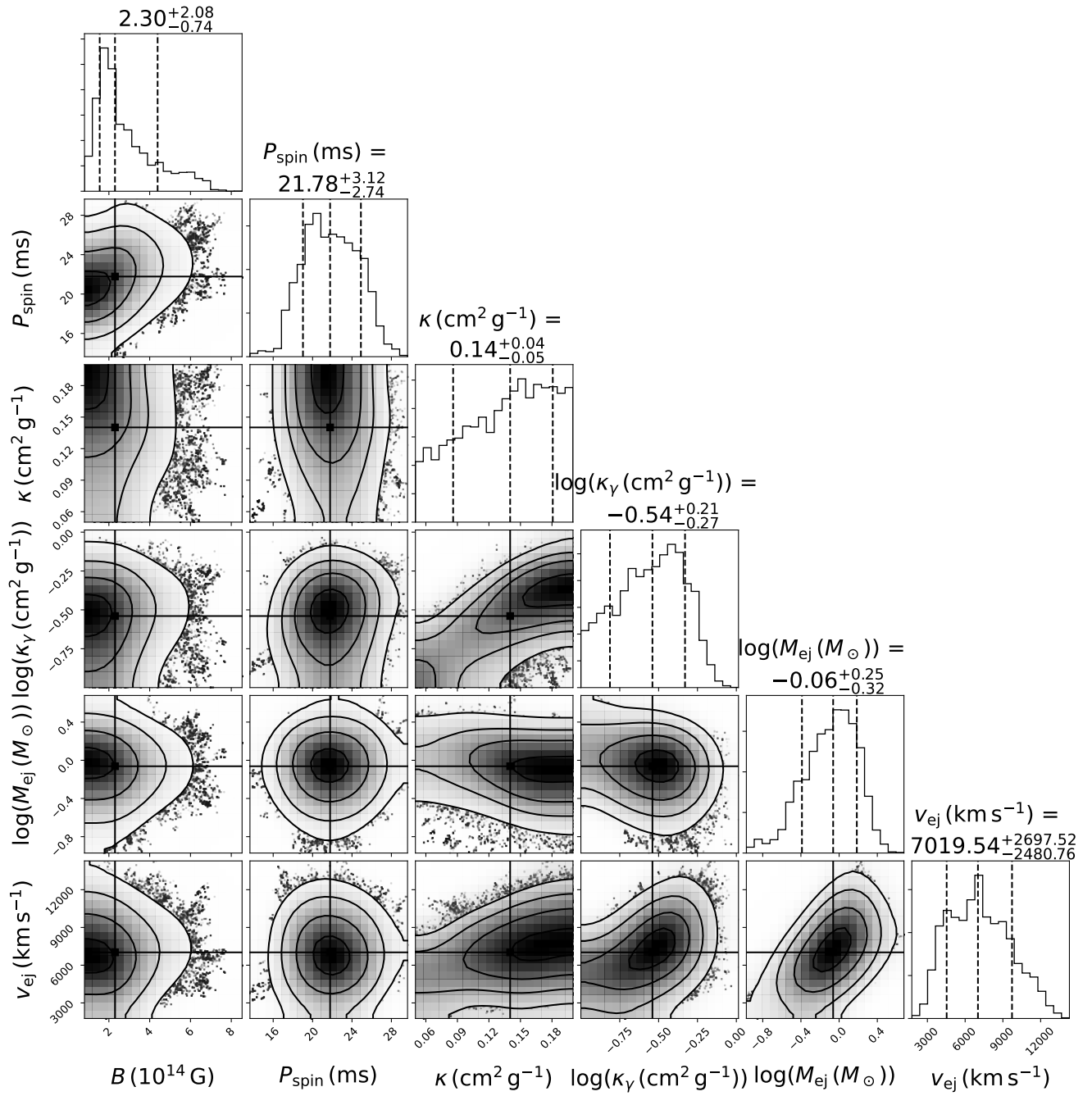


**Figure 15.** Posterior distributions of the best fit parameters of the models shown in Figure 6. Figure generated using corner (Foreman-Mackey 2016).